
GoRINNs: GODUNOV-RIEMANN INFORMED NEURAL NETWORKS FOR LEARNING HYPERBOLIC CONSERVATION LAWS

Dimitrios G. Patsatzis¹, Mario di Bernardo^{1,2}, Lucia Russo³, Constantinos Siettos^{4,*}

(¹)Modelling Engineering Risk and Complexity, *Scuola Superiore Meridionale*, Naples, Italy

(²)Dept. of Electrical Engineering and Information Technology, *University of Naples Federico II*, Naples, Italy

(³)Institute of Science and Technology for Energy and Sustainable Mobility,
Consiglio Nazionale delle Ricerche, Naples, Italy

(⁴)Dept. of Mathematics and Applications “Renato Caccioppoli”, *University of Naples Federico II*, Naples, Italy

November 1, 2024

ABSTRACT

We present GoRINNs: numerical analysis-informed neural networks for the solution of inverse problems of non-linear systems of conservation laws. GoRINNs are based on high-resolution Godunov schemes for the solution of the Riemann problem in hyperbolic Partial Differential Equations (PDEs). In contrast to other existing machine learning methods that learn the numerical fluxes of conservative Finite Volume methods, GoRINNs learn the physical flux function *per se*. Due to their structure, GoRINNs provide interpretable, conservative schemes, that learn the solution operator on the basis of approximate Riemann solvers that satisfy the Rankine-Hugoniot condition. The performance of GoRINNs is assessed via four benchmark problems, namely the Burgers’, the Shallow Water, the Lighthill-Whitham-Richards and the Payne-Whitham traffic flow models. The solution profiles of these PDEs exhibit shock waves, rarefactions and/or contact discontinuities at finite times. We demonstrate that GoRINNs provide a very high accuracy both in the smooth and discontinuous regions.

Keywords Numerical Analysis Informed Neural Networks · Riemann solvers · Godunov Scheme · Hyperbolic Partial Differential Equations · Conservation Laws · Interpretable Machine Learning

1 Introduction

Conservation laws (of mass, momentum, and energy) are fundamental physical laws present in many problems including fluid mechanics [4], traffic flow and crowd dynamics [5, 74], electromagnetism [53], among others, in which a physical quantity is conserved in time over an isolated spatial domain [18, 41]. The conserved quantities are physically determined or can arise in complex systems at the macroscopic level from the microscopic interactions (particles, molecules, vehicles, individuals, etc); see e.g., [11]. Conservation laws are often modelled with hyperbolic, (systems of) Partial Differential Equations (PDEs) [41], which can exhibit the challenging feature of emerging discontinuities, such as shock waves, at finite times even when the initial conditions are smooth [18].

As only a few (simple) hyperbolic PDEs exhibit analytic solutions, for real-world applications approximate solutions are sought via numerical methods that focus on accurately capturing the emerging discontinuities. For preserving the underlying conservation laws, the vast majority of numerical methods involve approximations of the numerical fluxes obtained by Finite Volume (FV) schemes [41], such as the Godunov and the Lax-Friedrichs schemes [27, 41]. The former allows for the employment of high-resolution methods such as flux-limiter methods [13, 71], which avoid non-physical solutions and peculiar oscillatory behavior around the discontinuities when suitable flux-limiters are used [41]. Most importantly, these schemes are conservative, under specific conditions related to the Riemann solver, such

*Corresponding author, email: constantinos.siettos@unina.it

as the *Rankine-Hugoniot* (RH) condition [41, 73]. Other methods include high-resolution (weighted) essential non-oscillatory (W)ENO schemes [29, 33], discontinuous Galerkin [26, 45] and spectral methods [78]. For a comprehensive presentation of FV numerical methods for conservation laws, see [7, 18, 35, 41] and references therein.

The solution of the so-called *forward* problem, has been the objective of many Scientific Machine Learning (SciML) algorithms. One broad category consists of physics-informed deep neural networks (PINNs) [52, 55, 62, 81] which however, when employed for hyperbolic PDEs, have a rather poor performance/low accuracy near the shock waves [50, 57]. To tackle this challenge, several PINN-based schemes have been proposed for respecting the conservation law [19, 57, 63, 82]. Finally, other methods include hybrid methods, which combine the classical numerical methods (to guarantee conservation) with neural networks (NNs) [37, 49, 68, 76, 77].

For the solution of the *inverse* problem (that is learning functional terms/closures/boundary conditions of unknown PDEs, as well as values of the parameters from available data), SciML methods typically include estimation of the time and spatial derivatives from time-series data, which are then provided in sparse regression models [34, 67, 69], DNNs [25, 40] and Gaussian Process Regressors [39, 61]. However, such schemes face significant challenges when employed to find closures of hyperbolic PDEs, since they do not preserve explicitly the conservation laws. In fact near shocks, the finite difference schemes for the estimation of the derivatives cannot accurately learn the true differential operator, and NN-based differentiation schemes may be required [3]. In addition, even when the derivative estimation is accurate, the above methods may introduce artificial differential terms in the related closures (see e.g. inviscid Burgers' equation in [69]). An alternative approach is the PINNs and their conservative flavors [1, 32, 50, 52, 55, 57, 81]. Neural Operators (NOs) such as DeepONets [46], Fourier Neural Operators [38, 43, 72], and RandONets [24], have been also introduced for learning the evolution operator, i.e. the right hand side of PDEs and/or the solution operator. However, NOs are also prone to discontinuities, and only few works are dedicated to hyperbolic PDEs [38, 79]. Recently, RiemannONets [60], a special variation of DeepONets [46], were introduced to approximate with high accuracy discontinuous solutions of the Riemann problem for hyperbolic equations.

While such schemes are highly accurate for parameter estimation tasks, they do not explicitly provide conservative schemes, nor have not so far been employed, to the best of our knowledge, for learning the functional closures in PDEs of conservation laws. For learning the flux functionals, hybrid methods have been recently developed, combining SciML algorithms with numerical methods [12, 36, 54]. The above hybrid methods are especially crafted for respecting conservation laws. However, they, learn the numerical approximation of the flux rather than the physical one. This may introduce significant inaccuracy for coarsely discretized data. For learning the physical, parameterized, flux, in [42], a special network architecture, resulting to rationals of polynomial functions, was coupled with the Rusanov (local Lax-Friedrichs) numerical FV scheme. Leaving aside the accuracy of the selected FV scheme (which is usually of first-order), all the aforementioned hybrid methods have been developed for non-linear scalar hyperbolic PDEs, in which the discontinuities (shocks) usually travel along one characteristic. Clearly, this is not the case for systems of hyperbolic PDEs.

In this work, we present a hybrid approach for the solution of the inverse problem for both scalar and systems of hyperbolic PDEs in 1-dim. spatial domains. In particular, we couple NNs with high-resolution Godunov-type FV schemes for the solution of the Riemann problem. We name this scheme as *Godunov-Riemann Informed Neural Networks (GoRINNs)*.

In contrast to existing hybrid methods that discover numerical fluxes [12, 36, 54], here we use shallow NNs to approximate directly the physical flux functional terms, which are missing from the flux function of the unknown system of PDEs. To take into account partial information that may be available, GoRINNs can be also employed in the presence of known fluxes or source terms in the system of PDEs. For obtaining the numerical solution of the unknown system, we perform operator splitting and solve the homogeneous part of the PDEs with high-resolution Godunov-type methods with flux-limiters and the inhomogeneous part (if any) with stiff integration schemes. These numerical schemes provide high-order accuracy both far and near the emerging discontinuities. However, since we deal with non-linear systems of hyperbolic PDEs, the related Riemann problem is solved by approximate Riemann solvers [41], which need to satisfy the *Rankine-Hugoniot* (RH) condition in order for the numerical scheme to be conservative [41, 73]. While NNs have been used to obtain accurate and RH condition-satisfying approximations for the solution of the Riemann problem via regression [49, 68, 76], here we solve the inverse problem with unknown flux terms; hence the target solutions are simply not available. To overcome this obstacle, we construct Riemann solvers that are dependent on the unknown flux function and constrain them to satisfy the RH condition; the latter is implemented as a soft constraint.

In this way, GoRINNs not only learn the physical unknown flux term/closures, but also the related approximate Riemann solver that renders the scheme conservative. This enables the direct implementation of GoRINNs into software packages for the solution of hyperbolic PDEs, as Clawpack [14], which require both the functional and the Riemann solver. This is the first time that such a hybrid approach for systems of conservation laws, is presented, allowing also the inclusion of source terms.

The performance of GoRINNs is assessed via four benchmark problems of non-linear conservation laws arising in fluid dynamics and traffic flow. First, we consider the scalar conservation laws of the inviscid Burgers' equation [9] and the Lighthill-Whitham-Richards (LWR) equation [44, 64], for which we learn the flux function and the velocity closure, respectively. Next, we study two systems of two conservation laws, the Shallow Water (SW) and the Payne-Whitham (PW) equations [59, 80], for both of which we learn the pressure closures in the flux function. We highlight here, that the Burgers', LWR and SW equations are homogeneous hyperbolic PDEs that exhibit analytic solutions for the Riemann problem, while for the PW equations not only the Riemann problem cannot be solved analytically, but also source terms are included. For all the benchmark problems, the approximate Riemann solvers are derived in appendix C. We underline here that for all problems under study, GoRINNs do not require extensive training data sets for achieving high approximation accuracy. This is because, a low number of complete (in space), time observations results in a high number of residuals to be minimized for the optimization problem, even for coarse spatial discretizations.

The reminder of the paper is organized as follows. In section 2, we concisely describe the problem definition. In section 3, we briefly present the high-resolution Godunov-type FV numerical scheme and introduce in detail GoRINNs for the solution of the inverse problem. In section 4, we present the numerical results for the four benchmark problems considered (which are presented in Appendix A along with details about the forward problem solution required for the data acquisition) and assess the convergence and accuracy of GoRINNs. Finally, in section 5, we conclude, discussing limitations and perspectives of the present work.

2 Problem Definition

We consider the general form of a system of D conservation laws, with the possible inclusion of source terms in an open domain Ω , and its boundary $\partial\Omega$. The evolution of conservative quantities $\mathbf{u} = \mathbf{u}(t, x) \in \mathbb{R}^D$ can be described by a non-homogeneous system of PDEs with prescribed initial and boundary conditions, in the form:

$$\partial_t \mathbf{u} + \partial_x \mathbf{f}(\mathbf{u}) = \mathbf{s}(\mathbf{u}) \text{ in } \Omega, \quad \mathbf{u}(0, x) = \mathbf{u}^0(x), \quad \mathcal{B}(\mathbf{u}(t, \partial\Omega)) = 0 \text{ on } \partial\Omega, \quad (1)$$

where $x \in \Omega$, and $\mathbf{f}(\mathbf{u}), \mathbf{s}(\mathbf{u}) : \mathbb{R}^D \rightarrow \mathbb{R}^D$ are continuously differentiable, non-linear functions, denoting the flux function and the source term, respectively. The system of PDEs in eq. (1) is hyperbolic iff the Jacobian matrix $\mathbf{J}(\mathbf{u}) = \partial_{\mathbf{u}} \mathbf{f}(\mathbf{u})$ is diagonalizable with real eigenvalues, for any $\mathbf{u} \in \mathbb{R}^D$.

Assuming the flux function $\mathbf{f}(\mathbf{u})$ and source term $\mathbf{s}(\mathbf{u})$ analytically available, deriving the solution of the system in eq. (1) is challenging due to the frequent occurrence of discontinuities (e.g., shock waves) emerging at finite times, even when the initial conditions are smooth functions [18, 41]. As discussed in section 1, classical numerical FV schemes, novel SciML methods, such as PINNs, NOs, or hybrid methods, can be used for deriving approximate solutions of the forward problem.

In this work, we aim at the solution of the inverse problem and effectively learn flux functionals/closures of the unknown PDE, given data of the state variables and partial information of about the system.

We consider the general form of the system in eq. (1) in the form:

$$\partial_t \mathbf{u} + \partial_x (\mathbf{f}_K(\mathbf{u}) + \mathbf{f}_U(\mathbf{u}, \mathcal{N}(\mathbf{u}))) = \mathbf{s}(\mathbf{u}), \quad (2)$$

where the flux term $\mathbf{f}(\mathbf{u}) = \mathbf{f}_K(\mathbf{u}) + \mathbf{f}_U(\mathbf{u}, \mathcal{N}(\mathbf{u}))$ consists of two continuously differentiable non-linear functions, the known $\mathbf{f}_K(\mathbf{u}) : \mathbb{R}^D \rightarrow \mathbb{R}^D$ and the unknown $\mathbf{f}_U(\mathbf{u}, \mathcal{N}(\mathbf{u})) : \mathbb{R}^D \rightarrow \mathbb{R}^D$. The unknown flux term includes a completely unknown functional of the state variables $\mathcal{N}(\mathbf{u}) : \mathbb{R}^D \rightarrow \mathbb{R}^D$, but may also include known functionals of \mathbf{u} . This particular form allows for the approximation of unknown flux functions for which partial (or desired) information may be available (e.g., when $\mathbf{f}_U(\mathbf{u}, \mathcal{N}(\mathbf{u})) = \mathbf{g}(\mathbf{u}) \cdot \mathcal{N}(\mathbf{u})$ with $\mathbf{g}(\mathbf{u})$ known).

As discussed in section 1, we shall approximate the unknown functional $\mathcal{N}(\mathbf{u})$ via shallow NNs, thus learning the physical/analytical flux $\mathbf{f}_U(\mathbf{u}, \mathcal{N}(\mathbf{u}))$, in contrast to existing hybrid methods that learn the numerical fluxes [12, 36, 54]. For learning $\mathcal{N}(\mathbf{u})$, we shall solve the forward problem for the system of the unknown system of PDEs in eq. (2), the solution of which generates the available data of the state variables.

3 Methodology: The GoRINNs

We present *Godunov-Riemann Informed Neural Networks* GoRINNs, a hybrid numerical analysis informed SciML scheme, for solving the inverse problem for hyperbolic systems of PDEs in the form of eq. (2), particularly for learning unknown flux terms. Our approach relies on the solution of the forward problem via high-resolution Godunov-type FV schemes, which, for the sake of completeness, we briefly describe below.

3.1 High-resolution Godunov-type methods

Consider the system in eq. (1), where the flux and source functionals are analytically known. For the solution of eq. (1), the numerical schemes require operator splitting for the homogeneous and inhomogeneous parts (if source terms are included). Typically, the homogeneous part is solved by FV schemes and then, the inhomogeneous part is integrated by implicit or explicit schemes, depending on the nature of $s(\mathbf{u})$ which can result in stiff problems. To numerically solve the homogeneous part, we employ high-resolution Godunov-type methods with flux-limiters, which allow for high-order accuracy near discontinuities and do not introduce non-physical solutions. More importantly, they are also conservative under conditions that will be discussed next. In fact, these methods are used in many Computational Fluid Dynamics software packages, such as COMSOL Multiphysics® [16], Clawpack [14], etc. For a comprehensive presentation of FV numerical methods for conservation laws, see [18, 35, 41].

For our illustration of employing a FV method, we will assume a 1-dim. spatial domain and its discretization in $i = 1, \dots, N$ FV cells, where the i -th cell occupies the space interval $[x_{i-1/2}, x_{i+1/2}]$, and assign the values of the state variables \mathbf{u} in eq. (1) as cell volumes, which we denote by \mathbf{Q}_i^n for the i -th cell at the n -th time step. Typically, the update of each \mathbf{Q}_i^n requires the solution of a *Riemann problem* with a contact discontinuity between a left and a right state, say $\mathbf{q}_l \in \mathbb{R}^D$ and $\mathbf{q}_r \in \mathbb{R}^D$ [65].

Here, since we use a Godunov's scheme [27] to solve the Riemann problem at each cell interface, the left and right states are given by adjacent cells at the n -th time step; i.e., $\mathbf{q}_l = \mathbf{Q}_{i-1}^n$ and $\mathbf{q}_r = \mathbf{Q}_i^n$. Then, the solution of the Riemann problem provides a set of M_w propagating waves, say $\mathbf{W}_{i-1/2}^p \in \mathbb{R}^D$, so that the contact discontinuity can be resolved as:

$$\Delta \mathbf{Q}_{i-1/2} \equiv \mathbf{Q}_i^n - \mathbf{Q}_{i-1}^n = \sum_{p=1}^{M_w} \mathbf{W}_{i-1/2}^p. \quad (3)$$

The waves travel through the left interface $i - 1/2$ of the i -th cell with characteristic speeds $s_{i-1/2}^p \in \mathbb{R}$, which may be negative or positive, say $(s_{i-1/2}^p)^-$ and $(s_{i-1/2}^p)^+$. A p -th negative/positive speed, indicates that the p -th wave propagates towards the left/right. As a result, left- and right-going fluctuations, $\mathcal{A}^- \Delta \mathbf{Q}_{i-1/2}$ and $\mathcal{A}^+ \Delta \mathbf{Q}_{i-1/2}$ respectively, are developed on the interface $i - 1/2$, which are given by:

$$\mathcal{A}^- \Delta \mathbf{Q}_{i-1/2} = \sum_{p=1}^{M_w} (s_{i-1/2}^p)^- \mathbf{W}_{i-1/2}^p, \quad \mathcal{A}^+ \Delta \mathbf{Q}_{i-1/2} = \sum_{p=1}^{M_w} (s_{i-1/2}^p)^+ \mathbf{W}_{i-1/2}^p, \quad (4)$$

and typically satisfy:

$$\mathcal{A}^- \Delta \mathbf{Q}_{i-1/2} + \mathcal{A}^+ \Delta \mathbf{Q}_{i-1/2} = \mathbf{f}(\mathbf{Q}_i^n) - \mathbf{f}(\mathbf{Q}_{i-1}^n), \quad (5)$$

in order for the solution to the Riemann problem to be conservative. With the definition of the fluctuations in eq. (4), a general high-resolution Godunov-type method provides the update of the value of the state variable \mathbf{Q}_i^{n+1} as:

$$\mathbf{Q}_i^{*,n+1} = \mathbf{Q}_i^n - \frac{\Delta t}{\Delta x} (\mathcal{A}^+ \Delta \mathbf{Q}_{i-1/2} + \mathcal{A}^- \Delta \mathbf{Q}_{i+1/2}) - \frac{\Delta t}{\Delta x} (\bar{\mathbf{F}}_{i+1/2} - \bar{\mathbf{F}}_{i-1/2}), \quad (6)$$

where the high-resolution corrections are:

$$\bar{\mathbf{F}}_{i-1/2} = \frac{1}{2} \sum_{p=1}^{M_w} |(s_{i-1/2}^p)^\pm| \left(1 - \frac{\Delta t}{\Delta x} |(s_{i-1/2}^p)^\pm| \right) \tilde{\mathbf{W}}_{i-1/2}^p. \quad (7)$$

The limited version of the p -th wave, $\tilde{\mathbf{W}}_{i-1/2}^p \in \mathbb{R}^D$, is computed via flux-limiter functions by comparing the wave $\mathbf{W}_{i-1/2}^p$ with the waves in adjacent cells; $\mathbf{W}_{i+1/2}^p$ for negative speeds $(s_{i-1/2}^p)^-$ or $\mathbf{W}_{i-3/2}^p$ for positive ones $(s_{i-1/2}^p)^+$. The use of flux-limiter functions (such as the minmod, superbee, Van Leer limiters) provides second-order accuracy to the numerical scheme and avoids non-physical peculiar oscillations near discontinuities or steep gradients [41].

Note that a necessary condition for the convergence of the Godunov-type method in eq. (6) is the satisfaction of the Courant-Friedrichs-Lowy (CFL) condition [17], which essentially restricts the time step Δt w.r.t. the cell length $\Delta x = x_{i+1/2} - x_{i-1/2}$ and the wave speeds, so that no wave is allowed to travel through more than one cell during the selected time step. As is evident from eq. (6), the update for the i -th cell requires the values of the state variables at adjacent cells, typically the $i - 2, \dots, i + 2$ cells. For the update of the cell with $i = 1, 2, N - 1, N$, the boundary conditions are taken into account, which are employed by augmenting the spatial domain, usually by two ghost cells per boundary; the values depend on the type of the boundary conditions, as discussed in detail in [41].

In the presence of source terms in eq. (1), the update $\mathbf{Q}_i^{*,n+1}$ resulting from the Godunov-type method in eq. (6), is then used as initial condition for the integration of the inhomogeneous part of the PDE. Thus, the value of the state variables at the next time step \mathbf{Q}_i^{n+1} is obtained by numerical integration of $d\mathbf{u}/dt = \mathbf{s}(\mathbf{u})$ with suitable schemes depending on the nature of $\mathbf{s}(\mathbf{u})$. A detailed discussion for the homogeneous/inhomogeneous operator splitting and the numerical integration schemes, is included on [41]. Naturally, $\mathbf{Q}_i^{n+1} = \mathbf{Q}_i^{*,n+1}$ in the absence of source terms.

Speeds and waves computation Given the numerical scheme in eq. (6), the solution of the forward problem, requires the computation of the speeds $s_{i-1/2}^p$ and the waves $\mathbf{W}_{i-1/2}^p$ from the known flux term $\mathbf{f}(\mathbf{u})$. The speeds and waves are provided by the solution of the Riemann problem, for which the so-called *Rankine-Hugoniot* (RH) jump condition should be satisfied [41] (determining the wave speeds and directions near jump discontinuities). For linear systems of hyperbolic PDEs, the RH condition implies that the speeds $s_{i-1/2}^p$ and the waves $\mathbf{W}_{i-1/2}^p$ can be computed by the p -th eigenvalue and the corresponding right eigenvector of the constant matrix $\mathbf{A} = \partial_{\mathbf{u}}\mathbf{f}(\mathbf{u})$. However, in a non-linear system the Riemann problem cannot be usually solved exactly, and thus approximate Riemann solvers are employed. An obvious choice is the linearized Riemann solver, for which it is assumed that the homogeneous system in eq. (1) can be locally approximated by:

$$\mathbf{u}_t + \hat{\mathbf{A}}_{i-1/2}\mathbf{u}_x = \mathbf{0}, \quad (8)$$

where $\hat{\mathbf{A}}_{i-1/2}$ is an approximation of the Jacobian $\mathbf{J}(\mathbf{u}) = \partial_{\mathbf{u}}\mathbf{f}(\mathbf{u})$ in the neighborhood of the $(i-1)$ -th and i -th cells. Hence, the speeds and waves computed via the eigenvalues and the eigenvectors of the linearized matrix $\hat{\mathbf{A}}_{i-1/2}$, can be provided into the numerical scheme of eq. (6). Note that $\hat{\mathbf{A}}_{i-1/2} \equiv \hat{\mathbf{A}}_{i-1/2}(\mathbf{q}_l, \mathbf{q}_r)$ and usually, as for the problems considered here, we are able to derive closed-form expressions for any \mathbf{q}_l and \mathbf{q}_r of the Riemann problem, hence accelerating computations.

In order for the linearized Riemann solver $\hat{\mathbf{A}}_{i-1/2}$ to guarantee that the numerical scheme in eq. (6) is conservative, and that the approximate Riemann solver is consistent with the exact one, the matrix $\hat{\mathbf{A}}_{i-1/2}(\mathbf{q}_l, \mathbf{q}_r)$ should, for every $\mathbf{q}_l, \mathbf{q}_r$, satisfy the following properties:

1. $\lim_{\mathbf{q}_l, \mathbf{q}_r \rightarrow \hat{\mathbf{q}}} \hat{\mathbf{A}}_{i-1/2}(\mathbf{q}_l, \mathbf{q}_r) = \mathbf{J}(\hat{\mathbf{q}}) = \partial_{\mathbf{u}}\mathbf{f}(\hat{\mathbf{q}})$, so that the solution of the linearized system in eq. (8) with the numerical scheme in eq. (6) is consistent with the solution of the non-linear conservation laws in eq. (1),
2. $\hat{\mathbf{A}}_{i-1/2}(\mathbf{q}_l, \mathbf{q}_r)$ diagonalizable with real eigenvalues, so that the linearized system in eq. (8) is hyperbolic, and,
3. $\hat{\mathbf{A}}_{i-1/2}(\mathbf{q}_l, \mathbf{q}_r) \cdot (\mathbf{q}_r - \mathbf{q}_l) = \mathbf{f}(\mathbf{q}_r) - \mathbf{f}(\mathbf{q}_l)$ (RH condition for systems), so that the solution of the linearized system in eq. (8) with the numerical scheme in eq. (6) is conservative.

The first two properties are essential for any approximate Riemann solver, while the third one is characteristic for a Roe solver [66]; it ensures that speeds calculated from the RH condition near contact discontinuities are in fact eigenvalues of the matrix $\hat{\mathbf{A}}_{i-1/2}$ and satisfy eq. (5).

The derivation of the Roe linearized matrix follows the general approach, introduced in [66], which includes a non-linear transformation of the state variables for a closed-form computation of the arising integrals. Alternatively, a “reverse engineering” approach [35] can be followed, in which one sets $\hat{\mathbf{A}}_{i-1/2}(\mathbf{q}_l, \mathbf{q}_r) = \partial_{\mathbf{u}}\mathbf{f}(\bar{\mathbf{q}})$ and seeks to find some *average* state $\bar{\mathbf{q}}$ as a function of \mathbf{q}_r and \mathbf{q}_l , such that the, related to RH condition, third property is satisfied. These techniques usually lead to same Roe matrices for many systems, albeit they are not always applicable; e.g., the second technique is not applicable for the fourth benchmark problem of PW equations (see Appendix C.4). This is because the flux function $\mathbf{f}(\mathbf{u})$ may not allow either the closed-form computation of the integrals involved in the first technique, or finding the average state $\bar{\mathbf{q}}$ involved in the second one; both techniques are presented in detail in Appendix B.

Finally, we note that while in many cases the Roe matrix $\hat{\mathbf{A}}_{i-1/2}$ is successfully used (with entropy fixes) for solving the forward problem, such kind of linearization may fail. In these cases, other approximate Riemann solvers should be used, e.g. the HLLE solver [23, 30], which effectively reduces to the Roe one when dealing with shock waves and does not require entropy fix when dealing with rarefactions. The disadvantage of the HLLE solver is that it is modelled by only two waves (i.e., $M_w = 2$ instead of $M_w = D$ in eq. (7)), which may affect the resolution of systems with more than two variables. A detailed presentation of the HLLE approximate Riemann solvers is also provided in Appendix B.

3.2 Solution of the inverse problem with GoRINNs

Here, we present *GoRINNs* for the solution of the inverse problem for scalar or systems of conservation laws described by hyperbolic PDEs. As already discussed, this is a hybrid approach combining the use of NNs with the high-resolution Godunov-type numerical methods presented in Section 3.1.

Let us first revisit the system of hyperbolic PDEs in eq. (2) with the unknown flux functionals term $\mathbf{f}_U(\mathbf{u}, \mathcal{N}(\mathbf{u}))$. For the approximation of the unknown functional, we consider a shallow NN, $\mathcal{N}(\mathbf{u}) := \mathcal{N}(\mathbf{u}, \mathbf{P}; \mathbf{H}_1) : \mathbb{R}^D \rightarrow \mathbb{R}^D$, with network parameters \mathbf{P} (weights and biases of each layer) and hyper-parameters \mathbf{H}_1 (e.g., activation function, learning rate, the number of epochs, etc.). To solve the inverse problem with GoRINNs, we seek to find the parameters \mathbf{P} of the NN $\mathcal{N}(\mathbf{u}, \mathbf{P}; \mathbf{H}_1)$, such that the employment of the high-resolution Godunov-type method of eq. (6) to the system in eq. (2) generates the available data for the values of the state variables.

GoRINNs as conservative schemes Recall that in order to employ a Godunov-type method, it is required to numerically compute the speeds and waves through an approximate Riemann solver of the linearized system in eq. (8). For guaranteeing a conservative and consistent with the non-linear system numerical scheme, we derive a Roe linearized matrix $\hat{\mathbf{A}}_{i-1/2}(\mathbf{q}_l, \mathbf{q}_r)$ for the unknown system of PDEs in eq. (2), which is required to satisfy the three properties discussed in Section 3.1. For the derivation of the Roe matrix, the general approach of [41] cannot be employed, since the integrals of the unknown flux term at transformed variables cannot be computed in a closed form. Hence, we follow a “reverse engineering” approach as proposed in [35], which results in the following proposition:

Proposition 1. *Consider the homogenous system of non-linear PDEs of eq. (2) with the partially known flux function $\mathbf{f}(\mathbf{u})$. Let $\mathbf{q}_l, \mathbf{q}_r \in \mathbb{R}^D$ be an arbitrary pair of left and right states of the related local Riemann problem and $\bar{\mathbf{q}} = \mathbf{h}(\mathbf{q}_l, \mathbf{q}_r)$ be an average state of them, such that $\hat{\mathbf{q}} = \mathbf{h}(\bar{\mathbf{q}}, \bar{\mathbf{q}})$ for $\hat{\mathbf{q}} \in \mathbb{R}^D$. Then, if the conditions:*

$$\partial_{\mathbf{u}} \mathbf{f}_K(\bar{\mathbf{q}}) \cdot (\mathbf{q}_r - \mathbf{q}_l) = \mathbf{f}_K(\mathbf{q}_r) - \mathbf{f}_K(\mathbf{q}_l), \quad (9)$$

$$(\partial_{\mathbf{u}} \mathbf{f}_U(\bar{\mathbf{q}}, \mathcal{N}(\bar{\mathbf{q}})) + \partial_{\mathcal{N}} \mathbf{f}_U(\bar{\mathbf{q}}, \mathcal{N}(\bar{\mathbf{q}})) \cdot \partial_{\mathbf{u}} \mathcal{N}(\bar{\mathbf{q}})) \cdot (\mathbf{q}_r - \mathbf{q}_l) = \mathbf{f}_U(\mathbf{q}_r, \mathcal{N}(\mathbf{q}_r)) - \mathbf{f}_U(\mathbf{q}_l, \mathcal{N}(\mathbf{q}_l)), \quad (10)$$

hold, the approximate Riemann solver defined by the Roe matrix $\hat{\mathbf{A}}_{i-1/2}(\mathbf{q}_l, \mathbf{q}_r) = \partial_{\mathbf{u}} \mathbf{f}(\bar{\mathbf{q}})$ satisfies the RH condition, and thus ensures that the Godunov-type numerical method in eq. (6) is conservative; the speeds and waves are computed from $\hat{\mathbf{A}}_{i-1/2}(\mathbf{q}_l, \mathbf{q}_r)$.

Proof. Using the definition of the known and unknown functions $\mathbf{f}(\mathbf{u}) = \mathbf{f}_K(\mathbf{u}) + \mathbf{f}_U(\mathbf{u}, \mathcal{N}(\mathbf{u}))$ included in the non-linear system of PDEs in eq. (2), the linearized matrix $\hat{\mathbf{A}}_{i-1/2}(\mathbf{q}_l, \mathbf{q}_r) = \partial_{\mathbf{u}} \mathbf{f}(\bar{\mathbf{q}})$ is written as:

$$\hat{\mathbf{A}}_{i-1/2}(\mathbf{q}_l, \mathbf{q}_r) = \partial_{\mathbf{u}} (\mathbf{f}_K(\bar{\mathbf{q}}) + \mathbf{f}_U(\bar{\mathbf{q}}, \mathcal{N}(\bar{\mathbf{q}}))) = \partial_{\mathbf{u}} \mathbf{f}_K(\bar{\mathbf{q}}) + \partial_{\mathbf{u}} \mathbf{f}_U(\bar{\mathbf{q}}, \mathcal{N}(\bar{\mathbf{q}})) + \partial_{\mathcal{N}} \mathbf{f}_U(\bar{\mathbf{q}}, \mathcal{N}(\bar{\mathbf{q}})) \cdot \partial_{\mathbf{u}} \mathcal{N}(\bar{\mathbf{q}}), \quad (11)$$

where the chain rule was employed at the last step. According to [66], the sufficient condition for rendering the Godunov-type numerical method in eq. (6) conservative is the RH condition:

$$\hat{\mathbf{A}}_{i-1/2}(\mathbf{q}_l, \mathbf{q}_r) \cdot (\mathbf{q}_r - \mathbf{q}_l) = \mathbf{f}(\mathbf{q}_r) - \mathbf{f}(\mathbf{q}_l), \quad (12)$$

which, upon substitution of eq. (11) yields:

$$(\partial_{\mathbf{u}} \mathbf{f}_K(\bar{\mathbf{q}}) + \partial_{\mathbf{u}} \mathbf{f}_U(\bar{\mathbf{q}}, \mathcal{N}(\bar{\mathbf{q}})) + \partial_{\mathcal{N}} \mathbf{f}_U(\bar{\mathbf{q}}, \mathcal{N}(\bar{\mathbf{q}})) \cdot \partial_{\mathbf{u}} \mathcal{N}(\bar{\mathbf{q}})) \cdot (\mathbf{q}_r - \mathbf{q}_l) = \mathbf{f}_K(\mathbf{q}_r) - \mathbf{f}_K(\mathbf{q}_l) + \mathbf{f}_U(\mathbf{q}_r, \mathcal{N}(\mathbf{q}_r)) - \mathbf{f}_U(\mathbf{q}_l, \mathcal{N}(\mathbf{q}_l)).$$

The latter equation should hold for any set of parameters included in $\mathbf{f}(\mathbf{u})$, both for known and unknown terms (e.g., the network parameters found in $\mathcal{N}(\mathbf{u})$). Its decomposition into known and unknown terms results in the sufficient for a conservative numerical method conditions of eqs. (9) and (10). \square

The construction of the Roe matrix $\hat{\mathbf{A}}_{i-1/2}$ with the conditions of Proposition 1 not only guarantees a conservative numerical scheme, but also satisfies by definition the first property regarding consistency in Section 3.1, since $\hat{\mathbf{A}}_{i-1/2}(\mathbf{q}_l, \mathbf{q}_r) \rightarrow \partial_{\mathbf{u}} \mathbf{f}(\hat{\mathbf{q}})$ as $\mathbf{q}_l, \mathbf{q}_r \rightarrow \hat{\mathbf{q}}$. However, for the construction of $\hat{\mathbf{A}}_{i-1/2}$, one needs to determine $\bar{\mathbf{q}} = \mathbf{h}(\mathbf{q}_l, \mathbf{q}_r)$ through the conditions in eqs. (9) and (10). In fact, the latter includes both the unknown flux term and the derivatives of the NN w.r.t. the state variables. Hence, $\bar{\mathbf{q}}$ can be partially determined as a function of \mathbf{q}_l and \mathbf{q}_r for only some of its components by solving eq. (9). For the rest of the components, we simply assume that they can be expressed by the arithmetic average $\bar{\mathbf{q}} = (\mathbf{q}_r + \mathbf{q}_l)/2$ and require eq. (10) to hold for the assumed $\bar{\mathbf{q}}$.

Let’s now assume a set of data points \mathbf{Q}_i^n at the n -th time step, discretized all over the 1-dim. spatial domain $[x_l, x_r]$ in $i = 1, \dots, N$ FV cells. Setting $\mathbf{q}_l = \mathbf{Q}_{i-1}^n$ and $\mathbf{q}_r = \mathbf{Q}_i^n$, one can estimate the averages $\bar{\mathbf{Q}}_i^n$ for every $i = 1, \dots, N$ by (i) computing the components of $\bar{\mathbf{q}}$ that can be determined from eq. (9) and (ii) making the assumption of the arithmetic average for the remaining components, as $\bar{\mathbf{Q}}_i^n = (\mathbf{Q}_{i-1}^n + \mathbf{Q}_i^n)/2$. Then, according to Proposition 1, the linearized Riemann solver of the unknown system of PDEs in eq. (2) is conservative if the condition in eq. (10) holds for every FV cell, that is:

$$(\partial_{\mathbf{u}} \mathbf{f}_U(\bar{\mathbf{Q}}_i^n, \mathcal{N}(\bar{\mathbf{Q}}_i^n)) + \partial_{\mathcal{N}} \mathbf{f}_U(\bar{\mathbf{Q}}_i^n, \mathcal{N}(\bar{\mathbf{Q}}_i^n)) \cdot \partial_{\mathbf{u}} \mathcal{N}(\bar{\mathbf{Q}}_i^n)) \cdot (\mathbf{Q}_i^n - \mathbf{Q}_{i-1}^n) = \mathbf{f}_U(\mathbf{Q}_i^n, \mathcal{N}(\mathbf{Q}_i^n)) - \mathbf{f}_U(\mathbf{Q}_{i-1}^n, \mathcal{N}(\mathbf{Q}_{i-1}^n)), \quad (13)$$

where the NN function is computed at $\bar{\mathbf{Q}}_i^n$, \mathbf{Q}_i^n and \mathbf{Q}_{i-1}^n . Finding the networks parameters that satisfy eq. (13) ensures that the proposed GoRINNs are conservative.

High-resolution GoRINNs Given the linearized Riemann solver $\hat{\mathbf{A}}_{i-1/2}(\mathbf{q}_l, \mathbf{q}_r) = \partial_{\mathbf{u}} \mathbf{f}(\bar{\mathbf{q}})$, the speeds and waves for the Godunov method can be estimated; for a Roe solver these are given by the eigenvalues and eigenvectors of $\hat{\mathbf{A}}_{i-1/2}$, while for an HLLE solver, one needs to compute a middle state of the Riemann problem as shown in Appendix B.2. In particular, for the high-resolution scheme in eq. (6), the update of i -th cell requires (i) the speeds $s_{i\pm 1/2}^p$ and waves $\mathbf{W}_{i\pm 1/2}^p$, which are functions of \mathbf{Q}_{i-1}^n , \mathbf{Q}_i^n and \mathbf{Q}_{i+1}^n and (ii) the flux-limited version of the waves, $\tilde{\mathbf{W}}_{i-1/2}^p$ and $\tilde{\mathbf{W}}_{i+1/2}^p$, which are functions of \mathbf{Q}_{i+a}^n for $a = -2, \dots, 2$, since $\tilde{\mathbf{W}}_{i-1/2}^p$ is a function of $\mathbf{W}_{i+1/2}^p$ and $\mathbf{W}_{i-3/2}^p$, and $\tilde{\mathbf{W}}_{i+1/2}^p$ is a function of $\mathbf{W}_{i+3/2}^p$ and $\mathbf{W}_{i-1/2}^p$. Hence, the FV high-resolution Godunov-type method in eq. (6) can be summarized as an update $\hat{\mathbf{Q}}_i^{n+1}$ of the form:

$$\hat{\mathbf{Q}}_i^{n+1} = FVG_{HR}(\mathbf{Q}_{i-2}^n, \mathbf{Q}_{i-2}^n, \mathbf{Q}_i^n, \mathbf{Q}_{i+1}^n, \mathbf{Q}_{i+2}^n, \mathbf{P}; \mathbf{H}_1, \mathbf{H}_2), \quad (14)$$

which depends on the parameters \mathbf{P} and hyperparameters \mathbf{H}_1 of the ANN (since the speeds and waves are computed via $\mathcal{N}(\mathbf{u}, \mathbf{P}; \mathbf{H}_1)$), but also on the hyperparameters \mathbf{H}_2 of the Godunov scheme, such as the flux-limited function, the type of solver (Roe, HLLE or others), etc. Note that the numerical scheme of eq. (14) requires information from the boundary conditions to update the $i = 1, 2, N-1, N$ nodes. As already discussed, two ghost cells are added to the left and right boundaries, the values of which are determined by the type of boundary condition; here, we assume that such information is available. Finally, note that the numerical scheme of eq. (14) also incorporates the numerical time integration scheme of the inhomogeneous splitted part, in cases where the system in eq. (2) includes source terms. The pseudocode for performing the update of eq. (14) is presented in detailed in Algorithm 1.

GoRINNs optimization problem Let's now assume the availability of n_t pairs of data points $\mathbf{Q}_i^n, \mathbf{Q}_i^{n+1}$ of the solution operator, over the entire 1-dim. spatial domain $[x_l, x_r]$; i.e., for $i = 1, \dots, N$. Then, the solution of the inverse problem is provided by the functional $\mathbf{f}_U(\mathbf{u}, \mathcal{N}(\mathbf{u}))$, for which the employment of the high-resolution Godunov-type update at \mathbf{Q}_i^n approximates \mathbf{Q}_i^{n+1} , under a conservative linearized Riemann solver. Hence, the numerical approximation of the unknown functional is provided by the parameters \mathbf{P} of the NN $\mathcal{N}(\mathbf{u}, \mathbf{P}; \mathbf{H}_1)$, computed by solving the optimization problem:

$$\min_{\mathbf{P}} \mathcal{L}(\mathbf{P}; \mathbf{H}_1, \mathbf{H}_2) := \sum_{n=1}^{n_t} (\|\mathcal{L}_{FVG}(\mathbf{Q}^{n+1}, \mathbf{Q}^n, \mathbf{P}; \mathbf{H}_1, \mathbf{H}_2)\|^2 + \|\mathcal{L}_{RH}(\mathbf{Q}^n, \mathbf{P}; \mathbf{H}_1)\|^2), \quad (15)$$

where $\mathcal{L}_{FVG}(\cdot)$ is the data loss function of the FV high-resolution Godunov update in eq. (14):

$$\mathcal{L}_{FVG}(\mathbf{Q}^{n+1}, \mathbf{Q}^n, \mathbf{P}; \mathbf{H}_1, \mathbf{H}_2) = \sum_{i=1}^N (\mathbf{Q}_i^{n+1} - FVG_{HR}(\mathbf{Q}_{i-2}^n, \mathbf{Q}_{i-2}^n, \mathbf{Q}_i^n, \mathbf{Q}_{i+1}^n, \mathbf{Q}_{i+2}^n, \mathbf{P}; \mathbf{H}_1, \mathbf{H}_2)), \quad (16)$$

and $\mathcal{L}_{RH}(\cdot)$ is the loss function soft constraining the satisfaction of the RH condition in eq. (13), as:

$$\begin{aligned} \mathcal{L}_{RH}(\mathbf{Q}^n, \mathbf{P}; \mathbf{H}_1) = & \sum_{i=1}^N \left((\partial_{\mathbf{u}} \mathbf{f}_U(\bar{\mathbf{Q}}_i^n, \mathcal{N}(\bar{\mathbf{Q}}_i^n, \mathbf{P}; \mathbf{H}_1)) + \partial_{\mathcal{N}} \mathbf{f}_U(\bar{\mathbf{Q}}_i^n, \mathcal{N}(\bar{\mathbf{Q}}_i^n, \mathbf{P}; \mathbf{H}_1)) \cdot \partial_{\mathbf{u}} \mathcal{N}(\bar{\mathbf{Q}}_i^n, \mathbf{P}; \mathbf{H}_1)) \cdot \right. \\ & \left. \cdot (\mathbf{Q}_i^n - \mathbf{Q}_{i-1}^n) - (\mathbf{f}_U(\mathbf{Q}_i^n, \mathcal{N}(\mathbf{Q}_i^n, \mathbf{P}; \mathbf{H}_1)) - \mathbf{f}_U(\mathbf{Q}_{i-1}^n, \mathcal{N}(\mathbf{Q}_{i-1}^n, \mathbf{P}; \mathbf{H}_1))) \right), \end{aligned} \quad (17)$$

for ensuring a conservative scheme. Here \mathbf{Q}^n denotes the values of state variables at the n -th time step for all $i = 1, \dots, N$ cells. Note that for minimizing the loss function in eq. (17), it is first required to compute the average states $\bar{\mathbf{Q}}_i^n$ from the data, as discussed after eq. (10).

GoRINNs implementation For the solution of the inverse problem with the GoRINNs, we employed a single-layer feedforward NN architecture with D -dim. inputs and 1-dim. output, since for all benchmark problems examined, a scalar flux function term was assumed unknown. For L neurons in the hidden layer, the output of the NN is written as:

$$\mathcal{N}(\mathbf{u}, \mathbf{P}; \mathbf{H}_1) = \mathbf{w}^o \top \phi(\mathbf{W}\mathbf{u} + \mathbf{b}), \quad (18)$$

where the network parameters $\mathbf{P} = [\mathbf{w}^o, \mathbf{W}, \mathbf{b}]^\top \in \mathbb{R}^{L(D+2)}$ include (i) the output weights $\mathbf{w}^o \in \mathbb{R}^L$ of the neurons between the output and the hidden layer, (ii) the internal weights $\mathbf{W} \in \mathbb{R}^{L \times D}$ between the hidden and the input layer, and (iii) the internal biases $\mathbf{b} \in \mathbb{R}^L$ of the neurons in the hidden layer. Output biases were not included, since they are not contributing in neither of the loss functions in eqs. (16) and (17); the derivative of the network w.r.t. \mathbf{u} appears in the former, and the difference between two NNs outputs in the latter. The outputs of the activated neurons are included

Algorithm 1 GoRINNs implementation

Require: Flux term $\mathbf{f}_K(\mathbf{u}) + \mathbf{f}_U(\mathbf{u}, \mathcal{N}(\mathbf{u}, \mathbf{P}; \mathbf{H}_1))$ and source term $\mathbf{s}(\mathbf{u})$ ▷ Known and unknown terms in eq. (2)

Require: State variables $\mathbf{Q}_{i-2}^n, \mathbf{Q}_{i-1}^n, \mathbf{Q}_i^n, \mathbf{Q}_{i+1}^n, \mathbf{Q}_{i+2}^n$, NN parameters \mathbf{P} and hyperparameters $\mathbf{H}_1, \mathbf{H}_2$

- 1: Get $D, N, \Delta t, \Delta x$, flux-limiter function $\phi(\theta)$, and type of boundary conditions included in \mathbf{H}_2
- 2: **if** $i = 1, 2, N-1, N$ **then**
- 3: Set values at required ghost cells $\mathbf{Q}_{-1}^n, \mathbf{Q}_0^n, \mathbf{Q}_{N+1}^n, \mathbf{Q}_{N+2}^n$ according to boundary conditions
- 4: ▷ Get numerical fluxes and high-resolution corrections at left and right interfaces $i-1/2$ and $i+1/2$ of the i -th cell △
- 5: Get left $\mathcal{A}^+ \Delta \mathbf{Q}_{i-1/2}, \bar{\mathbf{F}}_{i-1/2} \leftarrow \text{NUMERFLUX\&HRCOR}(\mathbf{Q}_{i-2}^n, \mathbf{Q}_{i-1}^n, \mathbf{Q}_i^n, \mathbf{Q}_{i+1}^n, \mathbf{P}, \mathbf{H}_1, \mathbf{H}_2)$
- 6: Get right $\mathcal{A}^- \Delta \mathbf{Q}_{i+1/2}, \bar{\mathbf{F}}_{i+1/2} \leftarrow \text{NUMERFLUX\&HRCOR}(\mathbf{Q}_{i-1}^n, \mathbf{Q}_i^n, \mathbf{Q}_{i+1}^n, \mathbf{Q}_{i+2}^n, \mathbf{P}, \mathbf{H}_1, \mathbf{H}_2)$
- 7: Get update $\mathbf{Q}_i^{*,n+1}$ ▷ Perform update in eq. (6)
- 8: **if** $\mathbf{s}(\mathbf{u}) \neq 0$ **then**
- 9: Integrate $d\mathbf{u}/dt = \mathbf{s}(\mathbf{u})$ with initial condition $\mathbf{Q}_i^{*,n+1}$ for Δt
- 10: Set $\hat{\mathbf{Q}}_i^{n+1} \leftarrow$ numerical solution ▷ Update in eq. (14)
- 11: **else**
- 12: Set $\hat{\mathbf{Q}}_i^{n+1} \leftarrow \mathbf{Q}_i^{*,n+1}$ ▷ Update in eq. (14)
- 13: ▷ Procedure to compute the numerical fluxes and high-resolution correction at $i-1/2$ interface, for given variable states $\mathbf{Q}_{i-2}^n, \mathbf{Q}_{i-1}^n, \mathbf{Q}_i^n, \mathbf{Q}_{i+1}^n$ at $i-2, i-1, i$ and $i+1$ cells, NN parameters \mathbf{P} and hyperparameters $\mathbf{H}_1, \mathbf{H}_2$
- 14: **procedure** $\text{NUMERFLUX\&HRCOR}(\mathbf{Q}_{i-2}^n, \mathbf{Q}_{i-1}^n, \mathbf{Q}_i^n, \mathbf{Q}_{i+1}^n, \mathbf{P}, \mathbf{H}_1, \mathbf{H}_2)$
- 15: Set left and right states $\mathbf{q}_l \leftarrow \mathbf{Q}_{i-1}^n$ and $\mathbf{q}_r \leftarrow \mathbf{Q}_i^n$ ▷ Numerical fluxes at $i-1/2$ interface
- 16: Get speeds and waves $s_{i-1/2}^p, \mathbf{W}_{i-1/2}^p \leftarrow \text{APPROXRIEMANNSOLVER}(\mathbf{q}_l, \mathbf{q}_r, \mathbf{P}, \mathbf{H}_1, \mathbf{H}_2)$
- 17: Compute numerical fluxes $\mathcal{A}^- \Delta \mathbf{Q}_{i-1/2}$ and $\mathcal{A}^+ \Delta \mathbf{Q}_{i-1/2}$ ▷ By eq. (4)
- 18: **for** $p = 1, \dots, M_w$ **do** ▷ High-resolution correction with flux-limiters
- 19: **if** $s_{i-1/2}^p < 0$ **then** ▷ Decide adjacent k -th cell
- 20: Set $k \leftarrow i, k_l \leftarrow k$ and $k_r \leftarrow k+1$
- 21: **else if** $s_{i-1/2}^p > 0$ **then**
- 22: Set $k \leftarrow i-1, k_l \leftarrow k-1$ and $k_r \leftarrow k$
- 23: Set left and right states $\mathbf{q}_l \leftarrow \mathbf{Q}_{k_l}^n$ and $\mathbf{q}_r \leftarrow \mathbf{Q}_{k_r}^n$ ▷ Waves at $k-1/2$ interface
- 24: Get waves $\mathbf{W}_{k-1/2}^p \leftarrow \text{APPROXRIEMANNSOLVER}(\mathbf{q}_l, \mathbf{q}_r, \mathbf{P}, \mathbf{H}_1, \mathbf{H}_2)$
- 25: Compute angle of waves $\theta^p \leftarrow \left((\mathbf{W}_{k-1/2}^p)^\top \cdot \mathbf{W}_{i-1/2}^p \right) / \left((\mathbf{W}_{i-1/2}^p)^\top \cdot \mathbf{W}_{i-1/2}^p \right)$.
- 26: Compute wave-limited version $\tilde{\mathbf{W}}_{i-1/2}^p \leftarrow \phi(\theta^p) \mathbf{W}_{i-1/2}^p$ via the flux-limiter function $\phi(\theta)$ ▷ By eq. (7)
- 27: Compute high-resolution correction $\bar{\mathbf{F}}_{i-1/2}$ ▷ By eq. (7)
- 28: **return** $\mathcal{A}^- \Delta \mathbf{Q}_{i-1/2}, \mathcal{A}^+ \Delta \mathbf{Q}_{i-1/2}$ and $\bar{\mathbf{F}}_{i-1/2}$ for $p = 1, \dots, M_w$
- 29: ▷ Procedure to compute the speeds and the waves provided by the approximate Riemann solver of the GoRINNs, for given left and right states $\mathbf{q}_l, \mathbf{q}_r$, NN parameters \mathbf{P} and hyperparameters $\mathbf{H}_1, \mathbf{H}_2$
- 30: **procedure** $\text{APPROXRIEMANNSOLVER}(\mathbf{q}_l, \mathbf{q}_r, \mathbf{P}, \mathbf{H}_1, \mathbf{H}_2)$
- 31: Compute $\bar{\mathbf{q}}$ from $\mathbf{q}_l, \mathbf{q}_r$ ▷ Partially by eq. (9) and partially by $(\mathbf{q}_l + \mathbf{q}_r)/2$
- 32: Compute $\partial_{\mathbf{u}} \mathcal{N}(\bar{\mathbf{q}}, \mathbf{P}; \mathbf{H}_1)$
- 33: Form linearized Roe matrix $\hat{\mathbf{A}}_{i-1/2}(\mathbf{q}_l, \mathbf{q}_r)$ ▷ By eq. (11)
- 34: Set $\mathbf{f}_{\text{sol}} \leftarrow \text{Roe}$ or HLLE from \mathbf{H}_2 ▷ Approximate Riemann solver type: Roe or HLLE
- 35: **if** $\mathbf{f}_{\text{sol}} = \text{ROE}$ **then**
- 36: Compute eigenvalues $\hat{\lambda}_{i-1/2}^p$ and eigenvectors $\hat{\mathbf{r}}_{i-1/2}^p$ of $\hat{\mathbf{A}}_{i-1/2}$ ▷ for $p = 1, \dots, D$
- 37: Set speeds $s_{i-1/2}^p \leftarrow \hat{\lambda}_{i-1/2}^p$ and waves $\mathbf{W}_{i-1/2}^p \leftarrow \hat{\mathbf{r}}_{i-1/2}^p$
- 38: **else if** $\mathbf{f}_{\text{sol}} = \text{HLLE}$ **then**
- 39: Compute $\mathcal{N}(\mathbf{q}_l) = \mathcal{N}(\mathbf{q}_l, \mathbf{P}; \mathbf{H}_1)$ and $\mathcal{N}(\mathbf{q}_r) = \mathcal{N}(\mathbf{q}_r, \mathbf{P}; \mathbf{H}_1)$ and derivatives w.r.t. \mathbf{u}
- 40: Form Jacobians $\mathbf{J}(\mathbf{q}_l) = \partial_{\mathbf{u}} (\mathbf{f}_K(\mathbf{q}_l) + \mathbf{f}_U(\mathbf{q}_l, \mathcal{N}(\mathbf{q}_l)))$ and $\mathbf{J}(\mathbf{q}_r) = \partial_{\mathbf{u}} (\mathbf{f}_K(\mathbf{q}_r) + \mathbf{f}_U(\mathbf{q}_r, \mathcal{N}(\mathbf{q}_r)))$
- 41: Compute eigenvalues $\hat{\lambda}_{i-1/2}^p, \lambda_{i-1}^p$ and λ_i^p of $\hat{\mathbf{A}}_{i-1/2}, \mathbf{J}(\mathbf{q}_l)$ and $\mathbf{J}(\mathbf{q}_r)$
- 42: Compute speeds $s_{i-1/2}^p$ for $p = 1, 2$ ▷ By eq. (B.5)
- 43: Compute middle state \mathbf{q}_m using $\mathcal{N}(\mathbf{q}_l)$ and $\mathcal{N}(\mathbf{q}_r)$ ▷ In eq. (B.6)
- 44: Compute waves $\mathbf{W}_{i-1/2}^p$ ▷ By eq. (B.7)
- 45: **return** $s_{i-1/2}^p$ and $\mathbf{W}_{i-1/2}^p$ for $p = 1, \dots, M_w$

in the column vector $\phi(\mathbf{W}\mathbf{u} + \mathbf{b}) \in \mathbb{R}^L$, for which the logistic sigmoid function is used as activation function. As already discussed, all hyperparameters are included in \mathbf{H}_1 .

For the solution of the GoRINNs optimization problem in eq. (15), the two loss functions in eqs. (16) and (17) were expressed in an $(D \times N \times n_t)$ -dim. and an $(N \times n_t)$ -dim. vector of non-linear residuals, say $\mathcal{F}_{FVG}(\mathbf{P})$ and $\mathcal{F}_{RH}(\mathbf{P})$, respectively. To minimize these residuals w.r.t. the unknown parameters \mathbf{P} , we used the Levenberg-Marquardt (LM) algorithm [28]. LM is a deterministic gradient-based optimization algorithm, which updates the unknown parameters according to a varying - at each iteration - damping factor λ . It thus, requires at each iteration the derivatives $\partial_{\mathbf{P}}\mathcal{F}_{FVG}$ and $\partial_{\mathbf{P}}\mathcal{F}_{RH}$. Since symbolic differentiation of $\partial_{\mathbf{P}}\mathcal{F}_{FVG}$ is not feasible, we used numerical differentiation through finite differences. Note that the residuals corresponding to eq. (16) can be computed independently for each $n = 1, \dots, n_t$, a feature that allowed us to perform parallel computations to form $\mathcal{F}_{FVG}(\mathbf{P})$ and thus accelerate convergence of the LM algorithm.

We highlight here an important feature of GoRINNs, related to the optimization problem and the LM algorithm employed for its solution. As discussed, GoRINNs are specifically designed with a linearized Riemann solver that renders the scheme conservative and consistent with the unknown non-linear system of conservation laws in eq. (2). However, there is no guarantee that the linearized system is hyperbolic, i.e., that the GoRINNs Roe matrix in eq. (11) is diagonalizable with real eigenvalues. To ensure hyperbolicity throughout the optimization process, one may include it as a hard constraint in the GoRINNs optimization problem in eq. (15), the solution of which would then require constrained optimization algorithms. Here, to avoid such algorithms, we initialized the LM algorithm with a random guess of the parameters \mathbf{P} , such that the Roe matrix in eq. (11) is diagonalizable with real eigenvalues. For ensuring hyperbolicity throughout the optimization process with the LM algorithm, a high value of the initial damping factor should be avoided for averting big steps in the parameter space, which may lead to loss of hyperbolicity.

3.3 Implementation and numerical assessment of GoRINNs

In this section, we provide all the practical details for the implementation and numerical assessment of GoRINNs, as employed for learning the unknown flux terms in the four benchmark problems considered.

For acquiring the data upon which GoRINNs are trained/tested on, we solved the forward problem for the known hyperbolic systems in the form of eq. (1) with well-posed initial data and boundary conditions. In particular, we consider two types of boundary conditions; either (i) periodic, in which the flow exits from the left/right boundary and enters from the right/left with the same characteristics, or (ii) outflow, in which the flow exits from the boundaries without reflections. For the former, we set the ghost cells to $\mathbf{Q}_{-1}^n = \mathbf{Q}_{N-1}^n$, $\mathbf{Q}_0^n = \mathbf{Q}_N^n$, $\mathbf{Q}_{N+1}^n = \mathbf{Q}_1^n$ and $\mathbf{Q}_{N+2}^n = \mathbf{Q}_2^n$ at every time step, while for the latter, we use zero-order extrapolation by setting $\mathbf{Q}_{-1}^n = \mathbf{Q}_0^n = \mathbf{Q}_1^n$ and $\mathbf{Q}_{N+1}^n = \mathbf{Q}_{N+2}^n = \mathbf{Q}_N^n$. For each problem, we consider smooth Gaussian or sinusoidal initial conditions $\mathbf{u}(0, x)$, which lead to shock waves and/or rarefactions along the time interval considered. For employing the high-resolution Godunov-type method described in Section 3.1, we compute the waves and speeds via the Roe linearized matrices derived for each problem, except from the fourth benchmark problem of the PW equations, for which the HLLE solver was used. In addition, in all problems, we used the Van-Leer flux-limiter function to derive the limited-versions of the waves in eq. (7). Finally, for the PW equations, where a source term is included in eq. (1), we used the stiff numerical integration scheme provided by *ode15s* of MATLAB ODE suite [70] for integrating the inhomogeneous part, as described in Section 3.1.

For each benchmark problem, we solved the forward problem for 4 different initial conditions in the $t \in [0, t_{end}]$ interval with different, for each problem, dt satisfying the CFL condition. From the collected data, we randomly split the 15-15-70% of the data to form the training, validation and testing sets; for the PW equations the split was 7.5-7.5-85% because the CFL-satisfying dt was smaller. The resulting sets consist of pairs of data points $\mathbf{Q}_i^n, \mathbf{Q}_i^{n+1} \in \mathbb{R}^D$ for all cells $i = 1, \dots, N$ and for randomly selected time steps $n = 1, \dots, n_t$. Only the training set was used for solving the GoRINNs optimization problem in eq. (15), which resulted in the formation of a total of $(D+1) \times N \times n_t$ residuals. We emphasize here that a larger training data set is not required, since only a few, complete time observations n_t are enough for forming many residuals, even with coarse spatial discretizations. For each problem, we determined n_t so that the ratio between the resulting number of residuals and the total number of trainable parameters in \mathbf{P} is ~ 5000 ; the number of neurons was set to $L = 5$, resulting to $5(D+2)$ trainable parameters.

As already discussed, for the GoRINNs optimization problem we used the LM algorithm over the training set, initialized with a random guess of parameters satisfying the hyperbolicity property of the Roe matrix in eq. (11) and an initial damping factor $\lambda_0 = 0.01$. The stopping criteria of the LM algorithm were (i) a maximum number of 500 epochs, (ii) a relative loss function (l^2) tolerance of 10^{-9} and (iii) a validation error below 10^{-9} for 3 consecutive iterations; the latter criterion was evaluated over the validation set in a frequency of 20 training epochs. To evaluate the convergence of the GoRINNs optimization problem, we computed the maximum and mean l^1 errors $\|\hat{\mathbf{Q}}_i^{n+1} - \mathbf{Q}_i^{n+1}\|_1$ and the

$MSE(\hat{\mathbf{Q}}_i^{n+1}, \mathbf{Q}_i^{n+1})$, over all cells $i = 1, \dots, N$, time steps $n = 1, \dots, n_t$, and state variable dimensions D ; $\hat{\mathbf{Q}}_i^{n+1}$ is the predicted value of the state variable at the next time step, as shown in eq. (14). An outline of the algorithm for the solution of the GoRINNs optimization problem with the LM iterative scheme is provided in Algorithm 2.

Algorithm 2 Outline of the solution of the GoRINNs optimization problem in eq. (15) with the LM algorithm

Require: Flux term $\mathbf{f}_K(\mathbf{u}) + \mathbf{f}_U(\mathbf{u}, \mathcal{N}(\mathbf{u}))$ and source term $\mathbf{s}(\mathbf{u})$ ▷ Known and unknown terms in eq. (2)

Require: State variables \mathbf{Q}^n and \mathbf{Q}^{n+1} for all n_t pairs and for all cells ▷ Training/validation data sets

- 1: Set hyperparameters \mathbf{H}_2 of the forward problem: $D, N, \Delta t, \Delta x$, flux-limiter function $\phi(\theta)$, type of boundary conditions and type of Riemann solver (ROE or HLLC)
- 2: Set NN hyperparameters \mathbf{H}_1 and randomly initialize NN parameters \mathbf{P} .
- 3: Set $isHyperbolic \leftarrow False$
- 4: **while** $isHyperbolic = False$ **do** ▷ Ensure hyperbolicity at initial parameters \mathbf{P}
- 5: **for** $i = 1, \dots, N$ and $n = 1, \dots, n_t$ **do**
- 6: Set $\mathbf{q}_l \leftarrow \mathbf{Q}_{i-1}^n$ and $\mathbf{q}_r \leftarrow \mathbf{Q}_i^n$; adjust with ghost cells when $i = 1, 2, N - 1, N$ ▷ Partially by eq. (9) and partially by $(\mathbf{q}_l + \mathbf{q}_r)/2$
- 7: Compute middle state $\bar{\mathbf{q}}$ from $\mathbf{q}_l, \mathbf{q}_r$ ▷ By eq. (11)
- 8: Compute $\partial_{\mathbf{u}}\mathcal{N}(\bar{\mathbf{q}}, \mathbf{P}; \mathbf{H}_1)$ and form linearized Roe matrix $\hat{\mathbf{A}}_{i-1/2}(\mathbf{q}_l, \mathbf{q}_r)$ ▷ By eq. (11)
- 9: **if** eigenvalues of $\hat{\mathbf{A}}_{i-1/2}$ are not real **then** Redraw randomly the parameters \mathbf{P} and go to line 3
- 10: Set $isHyperbolic \leftarrow True$

▷ Residual minimization with the LM algorithm

- 11: Set hyperparameters \mathbf{H}_2 of the LM algorithm: stopping criteria and initial damping factor λ_0
- 12: **repeat**
- 13: **for** $n = 1, \dots, n_t$ and $i = 1, \dots, N$ **do**
- 14: Compute $\hat{\mathbf{Q}}_i^{n+1} \leftarrow FVG_{HR}(\mathbf{Q}_{i-2}^n, \mathbf{Q}_{i-1}^n, \mathbf{Q}_i^n, \mathbf{Q}_{i+1}^n, \mathbf{Q}_{i+2}^n, \mathbf{P}; \mathbf{H}_1, \mathbf{H}_2)$ ▷ By eq. (14) and algorithm 1
- 15: Calculate loss $\mathbf{Q}_i^{n+1} - \hat{\mathbf{Q}}_i^{n+1}$ ▷ Loss function in eq. (16)
- 16: Form $(D \times N \times n_t)$ -dim. vector of residuals $\mathcal{F}_{FVG}(\mathbf{P})$
- 17: **for** $n = 1, \dots, n_t$ and $i = 1, \dots, N$ **do**
- 18: Set $\mathbf{q}_l \leftarrow \mathbf{Q}_{i-1}^n$ and $\mathbf{q}_r \leftarrow \mathbf{Q}_i^n$; adjust with ghost cells when $i = 1, 2, N - 1, N$ ▷ Partially by eq. (9) and partially by $(\mathbf{q}_l + \mathbf{q}_r)/2$
- 19: Compute middle state $\bar{\mathbf{q}}$ from $\mathbf{q}_l, \mathbf{q}_r$ ▷ By eq. (11)
- 20: Calculate loss $(\partial_{\mathbf{u}}\mathbf{f}_U(\bar{\mathbf{q}}, \mathcal{N}(\bar{\mathbf{q}}, \mathbf{P}; \mathbf{H}_1)) + \partial_{\mathbf{N}}\mathbf{f}_U(\bar{\mathbf{q}}, \mathcal{N}(\bar{\mathbf{q}}, \mathbf{P}; \mathbf{H}_1)) \cdot \partial_{\mathbf{u}}\mathcal{N}(\bar{\mathbf{q}}, \mathbf{P}; \mathbf{H}_1)) \cdot (\mathbf{q}_r - \mathbf{q}_l) - (\mathbf{f}_U(\mathbf{q}_r, \mathcal{N}(\mathbf{q}_r, \mathbf{P}; \mathbf{H}_1)) - \mathbf{f}_U(\mathbf{q}_l, \mathcal{N}(\mathbf{q}_l, \mathbf{P}; \mathbf{H}_1)))$ ▷ Loss function in eq. (17)
- 21: Form $(N \times n_t)$ -dim. vector of residuals $\mathcal{F}_{RH}(\mathbf{P})$
- 22: Obtain $\partial_{\mathbf{P}}\mathcal{F}_{FVG}(\mathbf{P})$ and $\partial_{\mathbf{P}}\mathcal{F}_{RH}(\mathbf{P})$ with numerical differentiation to form Jacobian matrix
- 23: Perform LM update [28] to get updated values of NN parameters \mathbf{P} and damping factor λ
- 24: **until** convergence
- 25: Get the final NN parameter values \mathbf{P}
- 26: Compute maximum and mean l^1 errors $\|\hat{\mathbf{Q}}_i^{n+1} - \mathbf{Q}_i^{n+1}\|_1$ and the $MSE(\hat{\mathbf{Q}}_i^{n+1}, \mathbf{Q}_i^{n+1})$, for all $i = 1, \dots, N$, $n = 1, \dots, n_t$, and D

Finally, to assess the numerical accuracy of GoRINNs, we solve the forward problem using the learned flux function $\mathbf{f}_U(\mathbf{u}, \mathcal{N}(\mathbf{u}))$ in eq. (2) and compare its solution $\hat{\mathbf{Q}}_i^{n+1}$ with the ground truth solution \mathbf{Q}_i^{n+1} of the forward problem for the analytically known flux function in eq. (1). To quantify the numerical accuracy, we use the absolute errors $|\hat{\mathbf{Q}}_i^{n+1} - \mathbf{Q}_i^{n+1}|$ all over cells and time steps for all the components of the state variables D . Note that this error is not the same with the training/validation/testing errors, since the solution of the forward problem with the learned flux function $\mathbf{f}_U(\mathbf{u}, \mathcal{N}(\mathbf{u}))$ also takes into account the cumulative error introduced by the numerical scheme.

All simulations were carried out with a CPU Intel(R) Core(TM) i7-13700H @ 2.40 GHz, RAM 32.0 GB using MATLAB R2022b with 14 parallel cores.

4 Numerical Results

In this section, we assess the performance of GoRINNs for the solution of the inverse problem for four benchmark problems of hyperbolic conservation laws. The first is the inviscid Burgers' equation [9], a benchmark problem in fluid mechanics end beyond (see e.g., [18, 35, 41]). The second problem, the Lighthill-Whitham-Richards (LWR) equation [44, 64], comes from the field of traffic flow, and shares many similarities with the Burgers' equation. Here, we consider it to demonstrate the use of GoRINNs on finding closures when partial information of the unknown flux function are available. For the next two problems, we consider two systems of $D = 2$ non-linear conservation laws; the Shallow

Water (SW) equations and the Payne-Whitham (PW) model. The SW equations can be derived by “depth-averaging” the Navier-Stokes equations for an incompressible and inviscid fluid under hydrostatic pressure. The SW equations consist one of the easiest systems to step up from scalar to systems of conservation laws. For all the above problems, the Riemann problem can be solved exactly [35, 41]. This is not the case for the last benchmark problem, the PW model [59, 80] of traffic flow, which describes a class of macroscopic second-order traffic models that take into account the individual behavior of the driver [31, 74]. We consider it here to demonstrate that GoRINNs can effectively handle hyperbolic systems with source terms.

For training the GoRINNs, we followed the procedure described in section 3.3 to collect training/validation/testing data sets from the numerical solutions of the analytically known hyperbolic PDEs. A presentation of the PDEs, and details on data acquisition, are provided in Appendix A. Next, we assessed the numerical accuracy of GoRINNs, by comparing the numerical solutions, provided by the high-resolution Godunov-type scheme in section 3.1, for the learned by GoRINNs, hyperbolic equation(s) and the analytically known equation(s) in Appendix A.

4.1 Learning the Burgers’ equation

Given the data set generated on the basis of the numerical solution of the Burgers’ equation in appendix A.1, a subset of which is depicted in fig. A.1a, we assume that the conservation law, from which they are originating, is written as:

$$\partial_t u + \partial_x \mathcal{N}(u) = 0, \quad (19)$$

where the flux function is completely unknown, thus corresponding to $f_K(u) = 0$, $f_U(u, \mathcal{N}(u)) = \mathcal{N}(u)$ and $s(u) = 0$ in eq. (2). To derive a Roe matrix for eq. (19) that satisfies the conditions of Proposition 1, eq. (9) does not provide any information about the average state \bar{q} , since $f_K(u) = 0$. We thus take the simple arithmetic average $\bar{q} = (q_l + q_r)/2$ and require eq. (10) to hold, yielding:

$$\partial_u \mathcal{N}(\bar{q})(q_r - q_l) = \mathcal{N}(q_r) - \mathcal{N}(q_l),$$

for any right and left states q_r, q_l in the data set. Then, the loss function in eq. (17) rendering GoRINNs conservative, reduces to:

$$\mathcal{L}_{RH}(\mathbf{Q}^n, \mathbf{P}; \mathbf{H}_1) = \sum_{i=1}^N \left((\partial_u \mathcal{N}(\bar{\mathbf{Q}}_i^n, \mathbf{P}; \mathbf{H}_1)) \cdot (\mathbf{Q}_i^n - \mathbf{Q}_{i-1}^n) - (\mathcal{N}(\mathbf{Q}_i^n, \mathbf{P}; \mathbf{H}_1) - \mathcal{N}(\mathbf{Q}_{i-1}^n, \mathbf{P}; \mathbf{H}_1)) \right), \quad (20)$$

which was used for solving the GoRINNs optimization problem in eq. (15).

As already discussed in section 3.3, we considered $L = 5$ neurons in the hidden layer and a logistic sigmoid activation function for learning the physical flux function $\mathcal{N}(u)$ with GoRINNs. The training results of GoRINNs are shown in table 1, where the maximum and mean $\|\hat{\mathbf{Q}}_i^{n+1} - \mathbf{Q}_i^{n+1}\|_1$ errors and the MSE($\hat{\mathbf{Q}}_i^{n+1}, \mathbf{Q}_i^{n+1}$) are reported over all $N = 100$ cells and $n_t = 360/360/1680$ (training/validation/testing) time steps. Clearly, the GoRINNs optimization scheme converges, since the maximum $\|\hat{\mathbf{Q}}_i^{n+1} - \mathbf{Q}_i^{n+1}\|_1$ error is of the order $1E - 06$.

Problem	max $\ \hat{\mathbf{Q}}_i^{n+1} - \mathbf{Q}_i^{n+1}\ _1$			mean $\ \hat{\mathbf{Q}}_i^{n+1} - \mathbf{Q}_i^{n+1}\ _1$			MSE($\hat{\mathbf{Q}}_i^{n+1}, \mathbf{Q}_i^{n+1}$)		
	Train	Val	Test	Train	Val	Test	Train	Val	Test
Burgers’	6.62E-06	5.38E-06	6.51E-06	3.60E-08	3.68E-08	3.63E-08	2.23E-14	2.23E-14	2.10E-14
LWR	5.15E-07	5.11E-07	5.34E-07	4.14E-09	3.68E-09	3.81E-09	3.30E-16	2.52E-16	2.98E-16
SW	1.08E-06	1.05E-06	1.04E-06	1.29E-08	1.21E-08	1.27E-08	1.35E-15	9.30E-16	1.24E-15
PW, $P(\rho, q)$	1.78E-03	1.78E-03	2.42E-03	6.77E-05	6.64E-05	6.56E-05	3.24E-08	3.24E-08	3.23E-08
PW, $P(\rho)$	8.71E-06	8.59E-06	9.51E-06	2.44E-07	2.45E-07	2.53E-07	3.73E-13	3.78E-13	3.94E-13

Table 1: Training, validation and testing errors of the GoRINNs optimization problem for all benchmark problems considered. The maximum and absolute $\|\hat{\mathbf{Q}}_i^{n+1} - \mathbf{Q}_i^{n+1}\|_1$ errors and the mean squared error MSE($\hat{\mathbf{Q}}_i^{n+1}, \mathbf{Q}_i^{n+1}$) are reported over all cells $i = 1, \dots, N$, time steps $n = 1, \dots, n_t$, and state variable dimensions D

The numerical accuracy of GoRINNs is visualized in fig. 1a,c. Figure 1a displays the absolute errors between the numerical solution, $\hat{u}(t, x)$, of eq. (19) with the learned by the GoRINNs flux functional $\mathcal{N}(u)$, and the ground truth one, $u(t, x)$, of the Burgers’ equation in eq. (A.1); the latter is the numerical solution displayed in fig. A.1a (in Appendix). As shown, the numerical accuracy provided by the GoRINNs is very high, even near the shock wave regions where the error is at most $6E - 05$. In addition, we demonstrate in fig. 1c that the flux functional learned by the GoRINNs is in excellent agreement with that of the Burgers’ equation $u^2/2$.

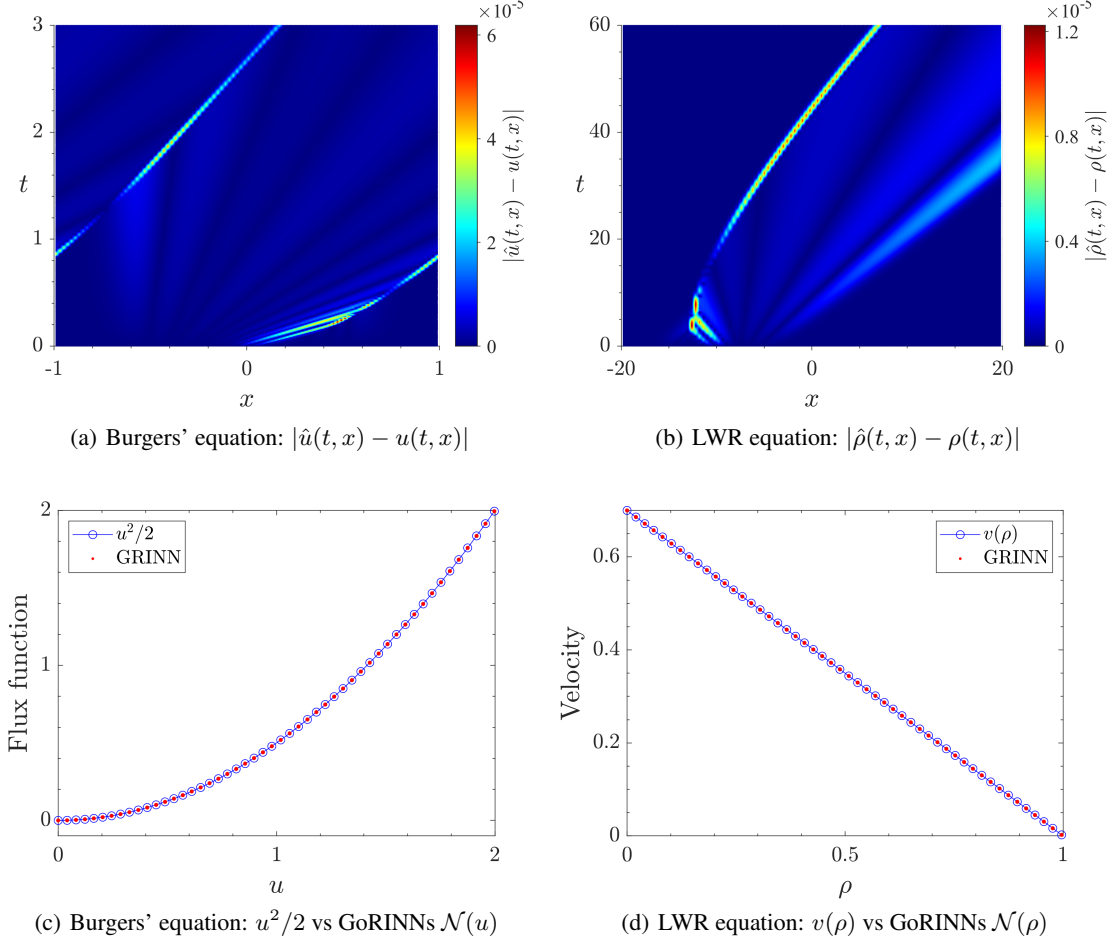


Figure 1: Numerical accuracy of GoRINNs for the Burgers' and LWR equations. (a,b) Absolute errors of the numerical solution provided by the GoRINNs learned equations in eqs. (19) and (21) (\hat{u} and $\hat{\rho}$) vs the one provided by Burgers' and LWR equations in eqs. (A.1) and (A.2) (u and ρ). (c,d) Analytically known flux function and velocity closure vs the $\mathcal{N}(u)/\mathcal{N}(\rho)$ functional learned by GoRINNs.

4.2 Learning the velocity closure of the LWR equation

Here, we assume that partial information regarding the conservation law is available, but we miss the velocity closure. In particular, given the set of data generated via the numerical solution of the LWR equation in appendix A.2, a subset of which is depicted in fig. A.1c, we assume that the originating equation is of the form:

$$\partial_t \rho + \partial_x (\rho \mathcal{N}(\rho)) = 0, \quad (21)$$

in which we seek to approximate the unknown velocity closure $v(\rho)$ by the NN $\mathcal{N}(\rho)$. Using the nomenclature in eq. (2), the unknown function is $f_U(\rho, \mathcal{N}(\rho)) = \rho \mathcal{N}(\rho)$ and $f_K(u) = s(u) = 0$. For deriving a Roe matrix of eq. (21) that satisfies the conditions of Proposition 1, eq. (9) does not provide any information about the average state $\bar{\rho}$, since $f_K(u) = 0$. As in the case of eq. (19), here we again assume the arithmetic average $\bar{\rho} = (\rho_l + \rho_r)/2$ and require eq. (10) to hold, which yields:

$$(\mathcal{N}(\bar{\rho}) + \bar{\rho} \partial_{\rho} \mathcal{N}(\bar{\rho})) (\rho_r - \rho_l) = \rho_r \mathcal{N}(\rho_r) - \rho_l \mathcal{N}(\rho_l),$$

for any right and left states ρ_r, ρ_l provided by the data set. Then, the loss function in eq. (17) rendering GoRINNs conservative, reduces to:

$$\mathcal{L}_{RH}(\mathbf{Q}^n, \mathbf{P}; \mathbf{H}_1) = \sum_{i=1}^N \left((\mathcal{N}(\bar{\mathbf{Q}}_i^n, \mathbf{P}; \mathbf{H}_1) + \bar{\mathbf{Q}}_i^n \cdot \partial_{\mathbf{u}} \mathcal{N}(\bar{\mathbf{Q}}_i^n, \mathbf{P}; \mathbf{H}_1)) \cdot (\mathbf{Q}_i^n - \mathbf{Q}_{i-1}^n) - (\mathbf{Q}_i^n \cdot \mathcal{N}(\mathbf{Q}_i^n, \mathbf{P}; \mathbf{H}_1) - \mathbf{Q}_{i-1}^n \cdot \mathcal{N}(\mathbf{Q}_{i-1}^n, \mathbf{P}; \mathbf{H}_1)) \right), \quad (22)$$

which was used for solving the GoRINNs optimization problem in eq. (15); similarly to the Burgers' equation, $L = 5$ neurons in the hidden layer and a logistic sigmoid activation function are considered for approximating $\mathcal{N}(\rho)$.

The training results are reported in table 1, again indicating that the GoRINNs optimization scheme converges. In particular, the maximum $\|\hat{\mathbf{Q}}_i^{n+1} - \mathbf{Q}_i^{n+1}\|_1$ error over all $N = 100$ cells and $n_t = 360/360/1680$ (training/validation/testing) time steps is around $5E - 07$.

For the assessment of the numerical accuracy of the GoRINNs, we compare in fig. 1b the numerical solution, $\hat{\rho}(t, x)$, of the unknown eq. (21) with the learned by the GoRINNs flux functional $\rho \mathcal{N}(\rho)$ and the ground true one, $\rho(t, x)$, of the LWR equation as shown in fig. A.1c. The differences are minor, with the absolute error being very low all over the time-space domain, even near the shock wave regions (the maximum there is $1.2E - 05$). We further demonstrate in fig. 1d that the velocity closure approximated by the GoRINNs is almost identical with the linear one of the LWR equation, $v(\rho) = v_{max}(1 - \rho)$.

4.3 Learning the pressure closure of the SW equations

For this problem, we consider the set of $D = 2$ -dim. data constructed on the basis of the numerical solution of the SW equations in appendix A.3, which consists of observations for h and q along the 1-dim. spatial domain $x \in [-5, 5]$; a subset of the training set is shown in fig. A.2a,b. We now assume that the conservation of mass is known, while the one of momentum is missing the pressure closure $P(h)$, which we seek to approximate with a NN $\mathcal{N}(h, q)$. We highlight here that the independence of the pressure by the momentum q is not a-priori known. Then, the unknown system of conservation laws is written in the form of eq. (2) as:

$$\partial_t \begin{bmatrix} h \\ q \end{bmatrix} + \partial_x \begin{bmatrix} q \\ \frac{q^2}{h} + \mathcal{N}(h, q) \end{bmatrix} = \begin{bmatrix} 0 \\ 0 \end{bmatrix}, \quad (23)$$

where the known flux term is $\mathbf{f}_K([h, q]^\top) = [q, q^2/h]^\top$ and the unknown one is simply composed by the NN as $\mathbf{f}_U([h, q]^\top) = [0, \mathcal{N}(h, q)]^\top$. To derive a Roe matrix for eq. (23) that satisfies the conditions of proposition 1, we first employ eq. (9) to get information for the average state $[\bar{h}, \bar{q}]^\top$. This results to a $D = 2$ -dim. system of equations, where the non-trivial one reads:

$$-\frac{\bar{q}^2}{\bar{h}^2}(h_r - h_l) + \frac{2\bar{q}}{\bar{h}}(q_r - q_l) = \frac{q_r^2}{h_r} - \frac{q_l^2}{h_l} \Rightarrow \bar{q} = \bar{h} \frac{q_l h_l^{-1/2} + q_r h_r^{-1/2}}{h_l^{1/2} + h_r^{1/2}}. \quad (24)$$

The above expression of \bar{q} agrees with the one of the SW equations in eq. (A.5). Now, given \bar{q} , we use the simple arithmetic average $\bar{h} = (h_r + h_l)/2$ and require eq. (10) to hold, which yields:

$$\partial_h \mathcal{N}(\bar{h}, \bar{q})(h_r - h_l) + \partial_q \mathcal{N}(\bar{h}, \bar{q})(q_r - q_l) = \mathcal{N}(h_r, q_r) - \mathcal{N}(h_l, q_l),$$

for any right and left states $(h_r, q_r), (h_l, q_l)$ provided by the data set. Then, the loss function in eq. (17) that renders GoRINNs conservative, reduces to:

$$\mathcal{L}_{RH}(\mathbf{Q}^n, \mathbf{P}; \mathbf{H}_1) = \sum_{i=1}^N \left(\partial_{\mathbf{u}} \mathcal{N}(\bar{\mathbf{Q}}_i^n, \mathbf{P}; \mathbf{H}_1) \cdot (\mathbf{Q}_i^n - \mathbf{Q}_{i-1}^n) - (\mathcal{N}(\mathbf{Q}_i^n, \mathbf{P}; \mathbf{H}_1) - \mathcal{N}(\mathbf{Q}_{i-1}^n, \mathbf{P}; \mathbf{H}_1)) \right), \quad (25)$$

where, in this benchmark problem, $\bar{\mathbf{Q}}_i^n$ requires only the computation of \bar{h} for every cell, since \bar{q} is given by eq. (24). We thus used the loss function in eq. (25) to solve the GoRINNs optimization problem in eq. (15). The approximation of the physical flux function $\mathcal{N}(h, q)$ shares the same architecture as in previous benchmark problems. The resulting training results are reported in table 1, where the small training/validation/testing errors indicate the convergence of the GoRINNs optimization scheme. In fact, the maximum $\|\hat{\mathbf{Q}}_i^{n+1} - \mathbf{Q}_i^{n+1}\|_1$ error over all $N = 200$ cells and $n_t = 180/180/840$ (training/validation/testing) time steps for both state variables $D = 1, 2$ is around $1E - 06$.

The numerical accuracy of GoRINNs is visualized in fig. 2. Figure 2a,b display the absolute errors, for each variable of the system, between the numerical solution of eq. (23) with the learned by the GoRINNs flux functional $\mathcal{N}(h, q)$ and the ground truth one, as computed from the SW equations in eq. (A.4); the latter is the numerical solution displayed in fig. A.2a,b. Again, the GoRINNs provide very high numerical accuracy for both h and q variables, even near the shock wave and rarefaction regions where the error is at most $1.5E-05$. In addition, the excellent agreement of the analytically known pressure closure, $P(h)$, and the GoRINNs learned functional, $\mathcal{N}(h, q)$, is displayed in fig. 2c. In fact, GoRINNs are capable to learn the independence of the pressure closure to q ; $\mathcal{N}(h, q)$ does not change along that q -axis.

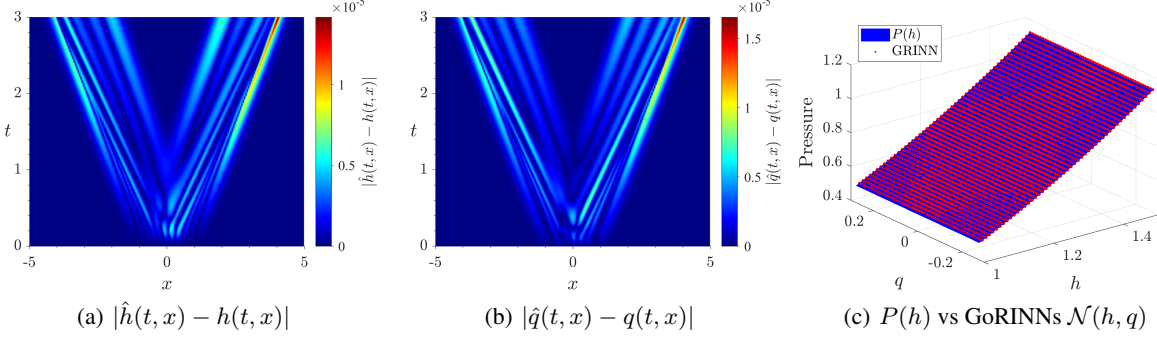


Figure 2: Numerical accuracy of GoRINNs for the SW equations. (a,b) Absolute errors of the numerical solution provided by the GoRINNs learned equations in eq. (23) (\hat{h} and \hat{q}) vs the one provided by SW equations in eq. (A.4) (h and q). (c) Analytically known pressure closure $P(h)$ vs the $\mathcal{N}(h, q)$ functional learned with GoRINNs.

4.4 Learning the pressure closure of the PW equations

In this problem, the data set that was constructed via the solution of the forward problem of the PW equations in appendix A.4, consists of a set of $D = 2$ -dim. observations for the density ρ and momentum q along the 1-dim. spatial domain $x \in [0, 800]$; a subset of these data is shown in fig. A.2d,e. As in the previous problem, the mass conservation is known, while the momentum conservation is lacking the pressure closure, which we seek to learn, without any a-priori knowledge on its variable dependencies, thus assuming that it can be approximated by a NN $\mathcal{N}(\rho, q)$. However, in this problem, we have information about the source term that renders the momentum equation inhomogeneous. With the above assumptions, the unknown system of conservation laws is written in the form of eq. (2) as:

$$\partial_t \begin{bmatrix} \rho \\ q \end{bmatrix} + \partial_x \begin{bmatrix} q \\ \frac{q^2}{\rho} + \mathcal{N}(\rho, q) \end{bmatrix} = \begin{bmatrix} 0 \\ \rho V_e(\rho) - q \end{bmatrix}, \quad (26)$$

where the known flux term is $\mathbf{f}_K([\rho, q]^\top) = [q, q^2/\rho]^\top$, the unknown one is $\mathbf{f}_U([\rho, q]^\top) = [0, \mathcal{N}(\rho, q)]^\top$ and the source term the same of the PW equations in eq. (A.6). Observe that the homogeneous system in eq. (26) is exactly the same as the one in eq. (23). Thus, similarly to eq. (24), for the Roe matrix we obtain by eq. (9) an average state:

$$-\frac{\bar{q}^2}{\bar{\rho}^2}(\rho_r - \rho_l) + \frac{2\bar{q}}{\bar{\rho}}(q_r - q_l) = \frac{q_r^2}{\rho_r} - \frac{q_l^2}{\rho_l} \Rightarrow \bar{q} = \bar{\rho} \frac{q_l \rho_l^{-1/2} + q_r \rho_r^{-1/2}}{\rho_l^{1/2} + \rho_r^{1/2}}, \quad (27)$$

which also agrees with the one of the known PW equations in eq. (A.9). According to Proposition 1, to render GoRINNs conservative, we again assume the arithmetic average $\bar{\rho} = (\rho_r + \rho_l)/2$ and require eq. (10) to hold, which implies the same simplified loss function as the one in eq. (25). We then use this loss function to solve the GoRINNs optimization problem in eq. (15).

The training results are reported in table 1; see row denoted as “PW, $P(\rho, q)$ ”. It is clearly shown that the GoRINNs optimization problem does not converge in as low values as in the other problems. In fact, the maximum $\|\hat{\mathbf{Q}}_i^{n+1} - \mathbf{Q}_i^{n+1}\|_1$ error over all $N = 100$ cells and $n_t = 360/360/4080$ (training/validation/testing) time steps for both state variables $D = 1, 2$, is not negligible; at the order of $\mathcal{O}(10^{-3})$. In fact, the pressure closure of the PW equations $P(\rho)$ is poorly approximated by the GoRINNs with $\mathcal{N}(\rho, q)$; see fig. D.1d. As a result, the numerical solution of eq. (26) is not accurate, as shown in fig. D.1a,b,c, especially near the shock wave where significant numerical errors accumulate.

This discrepancy occurs because the Roe linearized matrix $\hat{\mathbf{A}}_{i-1/2}(\mathbf{q}_l, \mathbf{q}_r)$ for the PW equations in eq. (A.9) does not result from the Jacobian $\partial_{\mathbf{u}}\mathbf{f}(\bar{\mathbf{q}})$ computed at the average state $\bar{\mathbf{q}} = [\bar{\rho}, \bar{\mathbf{q}}]^\top$; see discussion in Appendix C.4. In all other benchmark problems, the Roe linearized matrix $\hat{\mathbf{A}}_{i-1/2}(\mathbf{q}_l, \mathbf{q}_r)$ has this property and, thus, GoRINNs succeed to solve the inverse problem with a high accuracy.

When GoRINNs do not converge Clearly, when no information is available about the hyperbolic system from which the data come from, such an issue can only be captured by the incapability of GoRINNs to converge. The latter provides a hint on wrong predictor selection. We thus attempt to find desired pressure closure in eq. (26) as a function of only ρ and not q ; i.e., $\mathcal{N}(\rho)$.

By considering $\mathcal{N}(\rho)$ in eq. (26), GoRINNs are conservative when eqs. (9) and (10) in Proposition 1 are satisfied. Since no change is employed to the known functions, the average state \bar{q} is again provided by eq. (27). However, requiring eq. (10) to hold for the new $\mathbf{f}_U([\rho, q]^\top) = [0, \mathcal{N}(\rho)]^\top$, implies:

$$\partial_\rho \mathcal{N}(\bar{\rho})(\rho_r - \rho_l) = \mathcal{N}(\rho_r) - \mathcal{N}(\rho_l) \Rightarrow \partial_\rho \mathcal{N}(\bar{\rho}) = \frac{\mathcal{N}(\rho_r) - \mathcal{N}(\rho_l)}{\rho_r - \rho_l}. \quad (28)$$

The latter equality is similar to the one of the PW equation in eq. (A.9) and, in fact, allows us to substitute the above expression of $\partial_\rho \mathcal{N}(\bar{\rho})$ into the computation of the Roe linearized matrix of GoRINNs.

As a result, the RH condition is explicitly satisfied, and thus the GoRINNs optimization problem in eq. (15) can be solved without including the loss function term \mathcal{L}_{RH} in eq. (17), and without using the arithmetic average $\bar{\rho} = (\rho_r + \rho_l)/2$. The training results, derived by solving this simplified GoRINNs optimization problem, are reported in table 1; see row denoted as “PW, $P(\rho)$ ”. It is therein clearly shown that considering a density-dependent pressure closure makes the GoRINNs optimization problem converge to very small training/validation/testing errors. In fact, all errors are of magnitude, as low as the errors for the other benchmark problems.

The numerical accuracy of GoRINNs is visualized in fig. 3. Figure 3a,b display the absolute errors between the

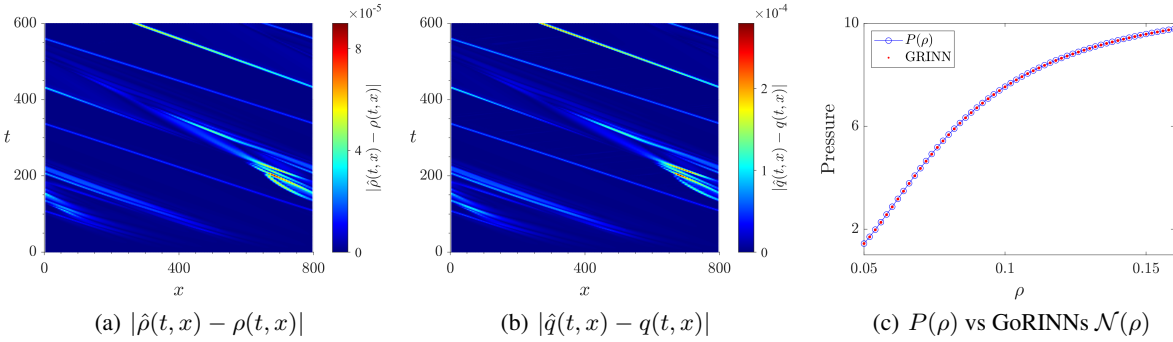


Figure 3: Numerical accuracy of GoRINNs, assuming a pressure closure of the form $\mathcal{N}(\rho)$, for the PW equations. (a,b) Absolute errors of the numerical solution provided by the GoRINNs learned equations in eq. (26) for $\mathcal{N}(\rho)$ ($\hat{\rho}$ and \hat{q}) vs the one provided by PW equations in eq. (A.6) (ρ and q). (c) Analytically known pressure closure $P(\rho)$ in eq. (A.7) vs the $\mathcal{N}(\rho)$ functional learned with GoRINNs.

numerical solution of eq. (26) with the learned by the GoRINNs density-dependent flux functional $\mathcal{N}(\rho)$ and the one computed from the PW equations in eq. (A.6); the latter numerical solution is displayed in fig. A.2d,e. Very high numerical accuracy is provided by the GoRINNs for both ρ and q variables, even near the shock wave and rarefaction regions. In these regions, the error was 2-3 orders higher when considering GoRINNs for a density $\mathcal{N}(\rho, q)$; see fig. D.1a,b. Finally, the excellent agreement of the analytically known non-linear pressure closure in eq. (A.7), $P(\rho)$, and the GoRINNs learned functional, $\mathcal{N}(\rho)$ is shown in fig. 3c.

5 Conclusions

Hyperbolic partial differential equations (PDEs) that model conservation laws play a central role in explaining complex phenomena across diverse disciplines such as fluid mechanics, aerospace engineering, electromagnetics, traffic flow, and crowd dynamics [5]. The numerical solution of the forward problem for such PDEs is challenging due to the presence of discontinuities, such as shock waves and rarefactions, which can cause classical numerical methods to fail

or yield inaccurate solutions. The inverse problem — i.e., that of learning the underlying closures/potentials or values of parameters in these PDEs from observed data — poses even greater difficulties as the problem is often ill-posed, thus relatively small approximation errors can lead to instabilities and violation of the conservation laws.

In the last few years, SciML deep-learning methods, such as PINNs [32, 50, 55, 57, 81] and neural operators [38, 46, 72, 79], have shown great potential in dealing with the challenging inverse problem of parameter inference in conservation laws. One critical issue is the lack of interpretability [21, 24, 60]. By construction most of the until now proposed schemes, set the conservation law as a soft constraint in the loss function, thus failing to respect accurately the conservation property. By explicitly preserving the conservation laws, hybrid SciML methods infer fluxes of conservative FV schemes [12, 36, 54], which however provide representation of the numerical-approximated quantities rather than the physical ones per se. These methods may introduce significant inaccuracies for coarsely discretized data and are developed for scalar conservation laws.

GoRINNs offer interpretable shallow feedforward NNs for tackling the above problems. Unlike other hybrid SciML methods that approximate the numerical fluxes, GoRINNs learn the solution of the Godunov scheme by directly approximating the physical flux functions per se. This approach enhances interpretability, thus respecting explicitly the underlying conservation laws as approximate Riemann solvers that satisfy the Rankine-Hugoniot condition. Moreover, GoRINNs provide a versatile framework for identifying flux functionals directly from data. This approach accommodates systems of conservation laws and allows for the inclusion of source terms—whether known or unknown—in the associated hyperbolic PDEs. As we show, GoRINNs are able to approximate accurately the closures of four benchmark problems, which exhibit traveling shocks that emerge at finite times. Based on the solution of the inverse problem, which actually approximates the physical flux function required for the solution operator of the Godunov-type scheme, we solved the forward problem for long time periods, showing that GoRINNs result to a high numerical approximation accuracy, preserving numerical stability and the conservation laws.

The training and performance of GoRINNs, like other SciML methods, benefit from partial knowledge of the physics underlying the missing terms (see section 4.4, where GoRINNs converge with the “correct” predictor selection.) If no physical insight is available, then techniques such as symbolic regression [6, 75], manifold learning (e.g., parsimonious diffusion maps) [15, 20, 22, 25, 56], and SINDy [8, 10] can be exploited to learn a parsimonious set of variables that can parametrize the unknown closures. Furthermore, GoRINNs can be extended to analyze real-world data derived from microscopic simulations/observations, facilitating the discovery of macroscopic hyperbolic PDEs for the emergent dynamics. This application will further require parameter inference, a task that can be addressed by including physical parameters as additional GoRINNs predictors. Finally, using GoRINNs to discover macroscopic closures connects directly to control theory, which can be exploited for enabling distributed control in large-scale microscopic models (see e.g., [47, 48]), given GoRINNs-derived information at the macroscopic level.

References

- [1] Ahmadi Daryakenari, N., De Florio, M., Shukla, K., and Karniadakis, G. E. (2024). Ai-aristotle: A physics-informed framework for systems biology gray-box identification. *PLOS Computational Biology*, 20(3):e1011916.
- [2] Bando, M., Hasebe, K., Nakayama, A., Shibata, A., and Sugiyama, Y. (1995). Dynamical model of traffic congestion and numerical simulation. *Physical review E*, 51(2):1035.
- [3] Bar-Sinai, Y., Hoyer, S., Hickey, J., and Brenner, M. P. (2019). Learning data-driven discretizations for partial differential equations. *Proceedings of the National Academy of Sciences*, 116(31):15344–15349.
- [4] Batchelor, G. K. (2000). *An introduction to fluid dynamics*. Cambridge university press.
- [5] Bellomo, N., Liao, J., Quaini, A., Russo, L., and Siettos, C. (2023). Human behavioral crowds review, critical analysis and research perspectives. *Mathematical Models and Methods in Applied Sciences*, 33(08):1611–1659.
- [6] Billard, L. and Diday, E. (2002). Symbolic regression analysis. In *Classification, clustering, and data analysis: recent advances and applications*, pages 281–288. Springer.
- [7] Bressan, A. (2000). *Hyperbolic systems of conservation laws: the one-dimensional Cauchy problem*, volume 20. Oxford University Press, USA.
- [8] Brunton, S. L., Proctor, J. L., and Kutz, J. N. (2016). Discovering governing equations from data by sparse identification of nonlinear dynamical systems. *Proceedings of the national academy of sciences*, 113(15):3932–3937.
- [9] Burgers, J. M. (1948). A mathematical model illustrating the theory of turbulence. *Advances in applied mechanics*, 1:171–199.
- [10] Champion, K., Lusch, B., Kutz, J. N., and Brunton, S. L. (2019). Data-driven discovery of coordinates and governing equations. *Proceedings of the National Academy of Sciences*, 116(45):22445–22451.

[11] Chapman, S. and Cowling, T. G. (1990). *The mathematical theory of non-uniform gases: an account of the kinetic theory of viscosity, thermal conduction and diffusion in gases*. Cambridge university press.

[12] Chen, Z., Gelb, A., and Lee, Y. (2024). Learning the dynamics for unknown hyperbolic conservation laws using deep neural networks. *SIAM Journal on Scientific Computing*, 46(2):A825–A850.

[13] Clain, S., Diot, S., and Loubère, R. (2011). A high-order finite volume method for systems of conservation laws—multi-dimensional optimal order detection (mood). *Journal of computational Physics*, 230(10):4028–4050.

[14] Clawpack Development Team (2024). Clawpack software. Version 5.10.0.

[15] Coifman, R. R. and Lafon, S. (2006). Diffusion maps. *Applied and computational harmonic analysis*, 21(1):5–30.

[16] COMSOL Inc. (2024). Comsol multiphysics. Version 6.2.

[17] Courant, R., Friedrichs, K., and Lewy, H. (1928). Über die partiellen differenzengleichungen der mathematischen physik. *Mathematische annalen*, 100(1):32–74.

[18] Dafermos, C. M. (2016). Hyperbolic conservation laws in continuum physics, 4th ed. In *Grundlehren der mathematischen Wissenschaften*. Springer Berlin, Heidelberg.

[19] De Ryck, T., Mishra, S., and Molinaro, R. (2024). wpinns: Weak physics informed neural networks for approximating entropy solutions of hyperbolic conservation laws. *SIAM Journal on Numerical Analysis*, 62(2):811–841.

[20] Della Pia, A., Patsatzis, D., Russo, L., and Siettos, C. (2024). Learning the latent dynamics of fluid flows from high-fidelity numerical simulations using parsimonious diffusion maps. *arXiv preprint arXiv:2408.02630*.

[21] Donecic, D. T., Mitsos, A., Guo, Y., Li, Q., Dietrich, F., Dahmen, M., and Kevrekidis, I. G. (2024). A recursively recurrent neural network (r2n2) architecture for learning iterative algorithms. *SIAM Journal on Scientific Computing*, 46(2):A719–A743.

[22] Dsilva, C. J., Talmon, R., Coifman, R. R., and Kevrekidis, I. G. (2018). Parsimonious representation of nonlinear dynamical systems through manifold learning: A chemotaxis case study. *Applied and Computational Harmonic Analysis*, 44(3):759–773.

[23] Einfeldt, B. (1988). On godunov-type methods for gas dynamics. *SIAM Journal on numerical analysis*, 25(2):294–318.

[24] Fabiani, G., Kevrekidis, I. G., Siettos, C., and Yannacopoulos, A. N. (2024). Randonet: Shallow-networks with random projections for learning linear and nonlinear operators. *arXiv preprint arXiv:2406.05470*.

[25] Galaris, E., Fabiani, G., Gallos, I., Kevrekidis, I., and Siettos, C. (2022). Numerical bifurcation analysis of pdes from lattice boltzmann model simulations: a parsimonious machine learning approach. *Journal of Scientific Computing*, 92(2):34.

[26] Girfoglio, M., Quaini, A., and Rozza, G. (2021). A pod-galerkin reduced order model for a les filtering approach. *Journal of Computational Physics*, 436:110260.

[27] Godunov, S. K. and Bohachevsky, I. (1959). Finite difference method for numerical computation of discontinuous solutions of the equations of fluid dynamics. *Matematicheskij sbornik*, 47(3):271–306.

[28] Hagan, M. T. and Menhaj, M. B. (1994). Training feedforward networks with the marquardt algorithm. *IEEE transactions on Neural Networks*, 5(6):989–993.

[29] Harten, A., Engquist, B., Osher, S., and Chakravarthy, S. R. (1997). Uniformly high order accurate essentially non-oscillatory schemes, iii. *Journal of computational physics*, 131(1):3–47.

[30] Harten, A., Lax, P. D., and Leer, B. v. (1983). On upstream differencing and godunov-type schemes for hyperbolic conservation laws. *SIAM review*, 25(1):35–61.

[31] Helbing, D. and Tilch, B. (1998). Generalized force model of traffic dynamics. *Physical review E*, 58(1):133.

[32] Jagtap, A. D., Kharazmi, E., and Karniadakis, G. E. (2020). Conservative physics-informed neural networks on discrete domains for conservation laws: Applications to forward and inverse problems. *Computer Methods in Applied Mechanics and Engineering*, 365:113028.

[33] Jiang, G.-S. and Shu, C.-W. (1996). Efficient implementation of weighted eno schemes. *Journal of computational physics*, 126(1):202–228.

[34] Kang, S. H., Liao, W., and Liu, Y. (2021). Ident: Identifying differential equations with numerical time evolution. *Journal of Scientific Computing*, 87:1–27.

[35] Ketcheson, D. I., LeVeque, R. J., and Del Razo, M. J. (2020). *Riemann problems and Jupyter solutions*, volume 16. SIAM.

[36] Kim, T. and Kang, M. (2024). Approximating numerical fluxes using fourier neural operators for hyperbolic conservation laws. *CoRR*.

[37] Kossaczká, T., Ehrhardt, M., and Günther, M. (2021). Enhanced fifth order weno shock-capturing schemes with deep learning. *Results in Applied Mathematics*, 12:100201.

[38] Kovachki, N., Li, Z., Liu, B., Azizzadenesheli, K., Bhattacharya, K., Stuart, A., and Anandkumar, A. (2023). Neural operator: Learning maps between function spaces with applications to pdes. *Journal of Machine Learning Research*, 24(89):1–97.

[39] Lee, S., Kooshbaghi, M., Spiliotis, K., Siettos, C. I., and Kevrekidis, I. G. (2020). Coarse-scale pdes from fine-scale observations via machine learning. *Chaos: An Interdisciplinary Journal of Nonlinear Science*, 30(1).

[40] Lee, S., Psarellis, Y. M., Siettos, C. I., and Kevrekidis, I. G. (2023). Learning black-and gray-box chemotactic pdes/closures from agent based monte carlo simulation data. *Journal of Mathematical Biology*, 87(1):15.

[41] LeVeque, R. J. (2002). *Finite volume methods for hyperbolic problems*, volume 31. Cambridge university press.

[42] Li, Q., Geng, J., and Evje, S. (2023). Identification of the flux function of nonlinear conservation laws with variable parameters. *Physica D: Nonlinear Phenomena*, 451:133773.

[43] Li, Z., Kovachki, N., Azizzadenesheli, K., Liu, B., Bhattacharya, K., Stuart, A., and Anandkumar, A. (2020). Fourier neural operator for parametric partial differential equations. *arXiv preprint arXiv:2010.08895*.

[44] Lighthill, M. J. and Whitham, G. B. (1955). On kinematic waves ii. a theory of traffic flow on long crowded roads. *Proceedings of the royal society of london. series a. mathematical and physical sciences*, 229(1178):317–345.

[45] Lomtev, I. and Karniadakis, G. E. (1999). A discontinuous galerkin method for the navier–stokes equations. *International journal for numerical methods in fluids*, 29(5):587–603.

[46] Lu, L., Jin, P., Pang, G., Zhang, Z., and Karniadakis, G. E. (2021). Learning nonlinear operators via deeponet based on the universal approximation theorem of operators. *Nature machine intelligence*, 3(3):218–229.

[47] Maffettone, G. C., Boldini, A., Di Bernardo, M., and Porfiri, M. (2022). Continuification control of large-scale multiagent systems in a ring. *IEEE Control Systems Letters*, 7:841–846.

[48] Maffettone, G. C., Liguori, L., Palermo, E., di Bernardo, M., and Porfiri, M. (2024). Mixed reality environment and high-dimensional continuification control for swarm robotics. *IEEE Transactions on Control Systems Technology*.

[49] Magiera, J., Ray, D., Hesthaven, J. S., and Rohde, C. (2020). Constraint-aware neural networks for riemann problems. *Journal of Computational Physics*, 409:109345.

[50] Mao, Z., Jagtap, A. D., and Karniadakis, G. E. (2020). Physics-informed neural networks for high-speed flows. *Computer Methods in Applied Mechanics and Engineering*, 360:112789.

[51] Marschler, C., Sieber, J., Berkemer, R., Kawamoto, A., and Starke, J. (2014). Implicit methods for equation-free analysis: Convergence results and analysis of emergent waves in microscopic traffic models. *SIAM Journal on Applied Dynamical Systems*, 13(3):1202–1238.

[52] Meng, X. and Karniadakis, G. E. (2020). A composite neural network that learns from multi-fidelity data: Application to function approximation and inverse pde problems. *Journal of Computational Physics*, 401:109020.

[53] Milton, K. and Schwinger, J. (2024). *Classical electrodynamics*. CRC Press.

[54] Morand, V., Müller, N., Weightman, R., Piccoli, B., Keimer, A., and Bayen, A. M. (2024). Deep learning of first-order nonlinear hyperbolic conservation law solvers. *Journal of Computational Physics*, 511:113114.

[55] Pang, G., Lu, L., and Karniadakis, G. E. (2019). fpinns: Fractional physics-informed neural networks. *SIAM Journal on Scientific Computing*, 41(4):A2603–A2626.

[56] Papapicco, D., Demo, N., Giroglio, M., Stabile, G., and Rozza, G. (2022). The neural network shifted-proper orthogonal decomposition: a machine learning approach for non-linear reduction of hyperbolic equations. *Computer Methods in Applied Mechanics and Engineering*, 392:114687.

[57] Patel, R. G., Manickam, I., Trask, N. A., Wood, M. A., Lee, M., Tomas, I., and Cyr, E. C. (2022). Thermodynamically consistent physics-informed neural networks for hyperbolic systems. *Journal of Computational Physics*, 449:110754.

[58] Patsatzis, D. G., Russo, L., Kevrekidis, I. G., and Siettos, C. (2023). Data-driven control of agent-based models: An equation/variable-free machine learning approach. *Journal of Computational Physics*, 478:111953.

[59] Payne, H. J. (1971). Model of freeway traffic and control. *Mathematical Model of Public System*, pages 51–61.

[60] Peyvan, A., Oommen, V., Jagtap, A. D., and Karniadakis, G. E. (2024). Riemannonet: Interpretable neural operators for riemann problems. *Computer Methods in Applied Mechanics and Engineering*, 426:116996.

[61] Raissi, M. and Karniadakis, G. E. (2018). Hidden physics models: Machine learning of nonlinear partial differential equations. *Journal of Computational Physics*, 357:125–141.

[62] Raissi, M., Perdikaris, P., and Karniadakis, G. E. (2019). Physics-informed neural networks: A deep learning framework for solving forward and inverse problems involving nonlinear partial differential equations. *Journal of Computational Physics*, 378:686–707.

[63] Rajvanshi, M. P. and Ketcheson, D. I. (2024). Integral pinns for hyperbolic conservation laws. In *ICLR 2024 Workshop on AI4DifferentialEquations In Science*.

[64] Richards, P. I. (1956). Shock waves on the highway. *Operations research*, 4(1):42–51.

[65] Riemann, B. (1860). *Über die Fortpflanzung ebener Luftwellen von endlicher Schwingungsweite*, volume 8. Verlag der Dieterichschen Buchhandlung.

[66] Roe, P. L. (1981). Approximate riemann solvers, parameter vectors, and difference schemes. *Journal of computational physics*, 43(2):357–372.

[67] Rudy, S. H., Brunton, S. L., Proctor, J. L., and Kutz, J. N. (2017). Data-driven discovery of partial differential equations. *Science advances*, 3(4):e1602614.

[68] Ruggeri, M., Roy, I., Mueterthies, M. J., Gruenwald, T., and Scalo, C. (2022). Neural-network-based riemann solver for real fluids and high explosives; application to computational fluid dynamics. *Physics of Fluids*, 34(11).

[69] Schaeffer, H. (2017). Learning partial differential equations via data discovery and sparse optimization. *Proceedings of the Royal Society A: Mathematical, Physical and Engineering Sciences*, 473(2197):20160446.

[70] Shampine, L. F. and Reichelt, M. W. (1997). The matlab ode suite. *SIAM journal on scientific computing*, 18(1):1–22.

[71] Sweby, P. K. (1984). High resolution schemes using flux limiters for hyperbolic conservation laws. *SIAM journal on numerical analysis*, 21(5):995–1011.

[72] Thodi, B. T., Ambadipudi, S. V. R., and Jabari, S. E. (2024). Fourier neural operator for learning solutions to macroscopic traffic flow models: Application to the forward and inverse problems. *Transportation research part C: emerging technologies*, 160:104500.

[73] Toro, E. F. (2013). *Riemann solvers and numerical methods for fluid dynamics: a practical introduction*. Springer Science & Business Media.

[74] Treiber, M. and Kesting, A. (2013). Traffic flow dynamics. *Traffic Flow Dynamics: Data, Models and Simulation*, Springer-Verlag Berlin Heidelberg, pages 983–1000.

[75] Udrescu, S.-M. and Tegmark, M. (2020). Ai feynman: A physics-inspired method for symbolic regression. *Science Advances*, 6(16):eaay2631.

[76] Wang, J. C.-H. and Hickey, J.-P. (2023). Fluxnet: a physics-informed learning-based riemann solver for transcritical flows with non-ideal thermodynamics. *Computer Methods in Applied Mechanics and Engineering*, 411:116070.

[77] Wang, Y., Shen, Z., Long, Z., and Dong, B. (2019). Learning to discretize: solving 1d scalar conservation laws via deep reinforcement learning. *arXiv preprint arXiv:1905.11079*.

[78] Wang, Z. J. (2007). High-order methods for the euler and navier–stokes equations on unstructured grids. *Progress in Aerospace Sciences*, 43(1-3):1–41.

[79] Wen, G., Li, Z., Azizzadenesheli, K., Anandkumar, A., and Benson, S. M. (2022). U-fno—an enhanced fourier neural operator-based deep-learning model for multiphase flow. *Advances in Water Resources*, 163:104180.

[80] Whitham, G. B. (2011). *Linear and nonlinear waves*. John Wiley & Sons.

[81] Yang, L., Zhang, D., and Karniadakis, G. E. (2020). Physics-informed generative adversarial networks for stochastic differential equations. *SIAM Journal on Scientific Computing*, 42(1):A292–A317.

[82] Zhang, X., Cheng, T., and Ju, L. (2022). Implicit form neural network for learning scalar hyperbolic conservation laws. In *Mathematical and Scientific Machine Learning*, pages 1082–1098. PMLR.

APPENDIX

A Benchmark problems and data acquisition

Here, we present the four benchmark problems upon which the performance of GoRINNs is evaluated on, namely the inviscid Burgers' equation, the LWR equation of traffic flow, the SW equations of fluid dynamics, and the PW equations of traffic flow. We additionally provide the details for the solution of the forward problem with the high-resolution Godunov-type FV scheme in section 3.1, which are required for the collection of training/validation/testing data sets.

A.1 Burger's equation

The inviscid Burgers' equation is one of the simplest problems of non-linear scalar conservation laws. Considering a homogeneous PDE with the non-linear flux term $f(u) = u^2/2$, the Burgers' equation is written in the form of eq. (1) as:

$$\partial_t u + \partial_x(u^2/2) = 0. \quad (\text{A.1})$$

Due to the simplicity of the Burgers' equation, the Riemann problem can be solved exactly [35, 41]. Here, we solve the Burgers' equation numerically in the 1-dim. spatial domain $x \in [-1, 1]$ with periodic boundary conditions, along the time interval $t \in [0, 3]$. In particular, we discretize the spatial domain in $N = 100$ cells and consider a time step $dt = 0.005$ that satisfies the CFL condition. As already discussed in section 3.3, for generating the numerical solutions, 4 different initial conditions were considered, all of which are following Gaussian profiles, with $u(0, x) = \mu \exp(-x^2/(2\sigma^2))$ for a constant $\sigma = 0.2$ and a uniformly varying $\mu \in [1, 2]$ with $d\mu = 1/3$.

In spite of the smooth initial conditions, contact discontinuities are formed within the selected time interval, in particular shock waves and rarefactions; the latter are not transonic due to the positive initial conditions. Thus, for the numerical solution of the forward problem via the Godunov-scheme in section 3.1, it is sufficient to employ the Roe solver, which leads to the scalar, in this case, Roe matrix $\hat{a}_{i-1/2} = \bar{u}$, where $\bar{u} = (u_l + u_r)/2$; the derivation is provided in appendix C.1. As already discussed in section 3.3, the Van-Leer flux-limiter function is employed. The resulting numerical solution of the Burgers' equation for the Gaussian initial data with $\mu = 2$ and $\sigma = 0.2$ is depicted in Figure A.1a,b, where it is clearly shown that the initial bump quickly forms a right going shock wave, followed by a rarefaction spread out towards the left; for comparison to the analytic solution, see Chapter 4 of [35]. From the 4 numerical solutions of the Burgers' equation, we randomly split the 15-15-70% of the time-series data to form the training/validation/testing data sets of the GoRINNs, as discussed in section 3.3; the training samples collected from the solution with initial data with $\mu = 2$ and $\sigma = 0.2$ are denoted with black circles in Figure A.1a.

A.2 LWR equation of traffic flow

The LWR equation [44, 64] is a non-linear scalar conservation law describing the evolution of the macroscopic density $\rho(t, x)$ of cars in a road. The traffic flow is modelled by the LWR equation in the form of eq. (1) as:

$$\partial_t \rho + \partial_x(\rho v(\rho)) = 0, \quad (\text{A.2})$$

where the car density $\rho(t, x) \in [0, 1]$ is moving with a density-dependent velocity:

$$v(\rho) = v_{max}(1 - \rho), \quad (\text{A.3})$$

where $v_{max} > 0$ is the maximum velocity, implying that $v(\rho) \in [0, v_{max}]$.

Similarly to the Burgers' equation, the Riemann problem for the LWR equation can be solved exactly [35, 41]. Here, we solve the LWR equation in eq. (A.2) numerically in the 1-dim. spatial domain $x \in [-20, 20]$ with outflow boundary conditions (allowing cars to exit the domain), along the time interval $t \in [0, 60]$. In particular, we set $v_{max} = 0.7$ and consider $N = 100$ cells and a time step $dt = 0.1$ that satisfies the CFL condition. As discussed in section 3.3, for generating the numerical solutions, 4 different initial conditions were considered, again following Gaussian profiles, this time forming an initial bump around $x_0 = -10$; that is, we set $\rho(0, x) = \mu \exp(-(x - x_0)^2/(2\sigma^2))$ for a constant $\mu = 1$ and a uniformly varying $\sigma \in [1, 2.5]$ with $d\sigma = 0.5$.

Similarly to the Burgers' equation, in spite of the smooth initial conditions, contact discontinuities are formed within the selected time interval. For the numerical solution via the Godunov-scheme in section 3.1, it is sufficient to employ the Roe solver. The scalar, for the LWR equation, Roe matrix takes the form $\hat{a}_{i-1/2} = v_{max}(1 - 2\bar{\rho})$, where $\bar{\rho} = (\rho_l + \rho_r)/2$; see the derivation in appendix C.2. The resulting numerical solution of the LWR equation, using the Van-Leer flux-limiter function, for the Gaussian initial conditions with $\sigma = 2$ is depicted in Figure A.1c,d. In contrast to the Burgers' equation, the non-linear flux term of the LWR equation $f(\rho) = v_{max}\rho(1 - \rho)$ is not convex, but concave. Because of that, as shown in Figure A.1c, the initial smooth profiles quickly form a right going shock wave, which is now following

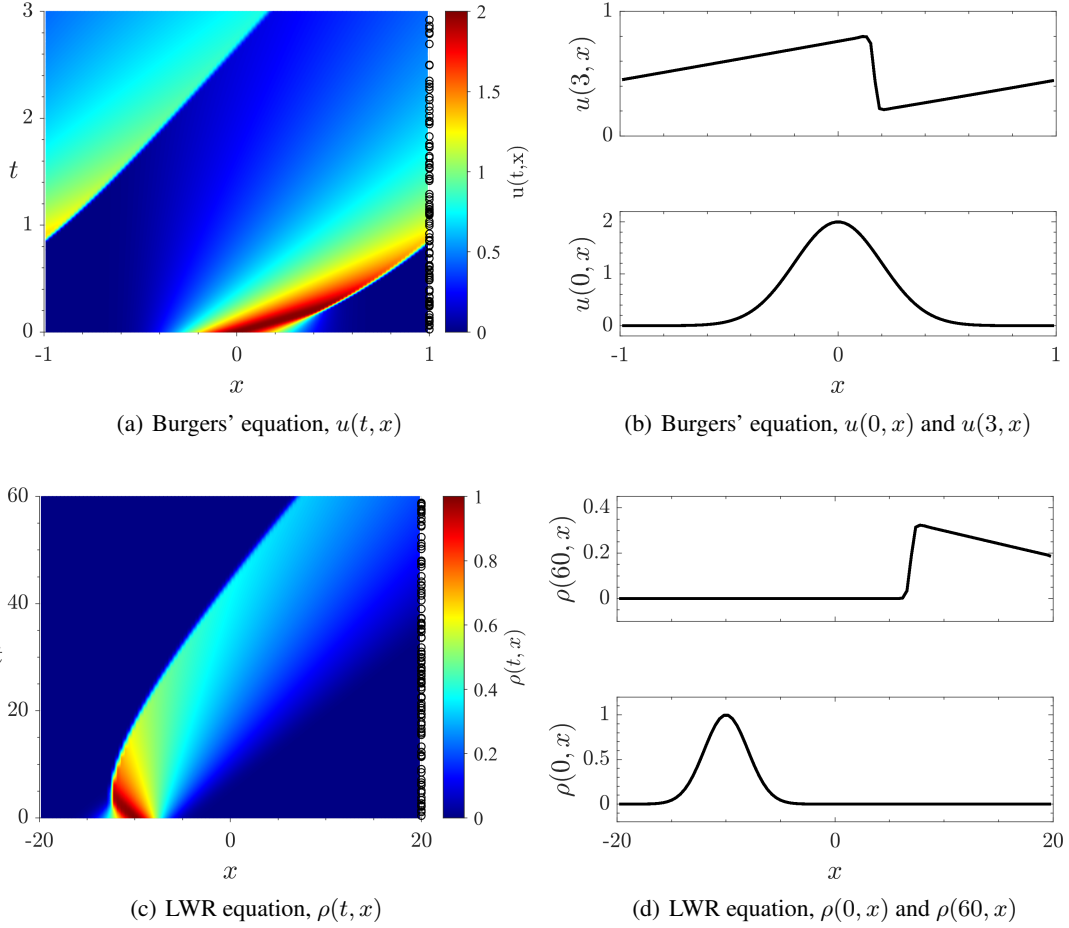


Figure A.1: Numerical solution of the Burgers' and LWR equations obtained with the high-resolution Godunov-scheme in section 3.1 for (a,b) $x \in [-1, 1]$, $t \in [0, 3]$, with the initial data $u(0, x) = 2 \exp(-x^2/(2 \cdot 0.2^2))$ shown in panel (b), and (c,d) $x \in [-20, 20]$, $t \in [0, 60]$ with the $\rho(0, x) = \exp(-(x + 10)^2/(2 \cdot 2^2))$ shown in panel (d). Periodic boundary conditions are used for the Burgers' equation and outflow ones for the LWR equation. The black circles on (a,c) denote the time steps n_t , collected from the depicted numerical solutions, to form the training set of GoRINNs.

the right-spreading rarefaction (instead of preceding it, as shown in Figure A.1a for the Burgers' equation). This behavior is well aligned with the relaxation of traffic jams reported for agent-based car-following models; see Chapter 11 of [41] for a direct comparison. From the 4 numerical solutions of the LWR equation, we randomly split the 15-15-70% of the time-series data to form the training/validation/testing data sets of the GoRINNs, as discussed in section 3.3; the training samples collected from the solution with initial data with $\mu = 1$ and $\sigma = 2$ are denoted with black circles in Figure A.1c.

A.3 The SW equations

The SW equations is a system of $D = 2$ non-linear conservation laws describing the flow of an incompressible and inviscid fluid below a pressure surface. The conservation of mass and momentum in 1 dimension is then modeled by the SW equations in the form of eq. (1) as:

$$\partial_t \begin{bmatrix} h \\ q \end{bmatrix} + \partial_x \begin{bmatrix} q \\ \frac{q^2}{h} + P(h) \end{bmatrix} = \begin{bmatrix} 0 \\ 0 \end{bmatrix} \quad (\text{A.4})$$

where $h(t, x)$ and $q(t, x)$ are the depth and momentum conservative state variables. The pressure is assumed to be hydrostatic, thus taking the depth-dependent form $P(h) = (gh^2)/2$ where $g > 0$ is a rescaled parameter of the gravitational constant.

Although the Riemann problem for the SW equations can be solved exactly [35, 41], here we numerically solve the system in eq. (A.4) in the 1-dim. spatial domain $x \in [-5, 5]$ with periodic boundary conditions, along the time interval $t \in [0, 3]$. In particular, we set $g = 1$ and consider $N = 200$ cells and a, CFL satisfying, time step $dt = 0.01$. For generating the data, we considered 4 initial conditions, following again Gaussian profiles for $h(0, x)$; we set $h(0, x) = \mu \exp(-x^2/(2\sigma^2))$ for a constant $\mu = 0.5$ and a uniformly varying $\sigma \in [0.2, 0.8]$ with $d\sigma = 0.2$, and $q(0, x) = 0$.

Starting from the aforementioned smooth initial data, the SW equations exhibit contact discontinuities within the selected time interval. Since they are not transonic rarefactions, but only shock waves and rarefactions, it is sufficient to employ the Roe solver for obtaining the numerical solution via the Godunov-scheme in section 3.1; for transonic rarefactions the HLLE solver can be employed instead. The Roe linearized matrix for the SW equations is:

$$\hat{\mathbf{A}}_{i-1/2} = \begin{bmatrix} 0 & 1 \\ -\bar{q}^2 & \bar{h} \\ \frac{1}{\bar{h}^2} + g\bar{h} & 2\bar{q} \end{bmatrix}, \quad \text{where} \quad \bar{h} = \frac{h_l + h_r}{2}, \quad \bar{q} = \bar{h} \frac{q_l h_l^{-1/2} + q_r h_r^{-1/2}}{h_l^{1/2} + h_r^{1/2}}, \quad (\text{A.5})$$

the latter being the so-called *Roe average*. For the derivation of $\hat{\mathbf{A}}_{i-1/2}$, which is presented in detail in appendix C.3, we followed the general approach introduced by [66], resulting in the same Roe matrix as the ones derived in [35, 41]. The resulting numerical solution of the SW equations, using the Van-Leer flux-limiter function, for the Gaussian initial data with $\sigma = 0.4$ is depicted in Figure A.2a,b,c for h and q , respectively. It is therein shown that after a fast transient period, the initially smooth data form one left and one right going shock waves, which are followed by rarefactions spreading towards the opposite direction of the shock wave movement. In fact, h is symmetric along the spatial domain, while q is antisymmetric; see Figure A.2c. From the 4 numerical solutions of the SW equations, we randomly split the 15-15-70% of the time-series data to form the training/validation/testing data sets of the GoRINNs, as discussed in section 3.3; the training samples collected from the solution with initial data with $\mu = 0.5$ and $\sigma = 0.4$ are denoted with black circles in Figure A.2a,b.

A.4 The PW equations of traffic flow

The PW equations [59, 80] is a system of $D = 2$ non-linear conservation laws, describing a class of macroscopic second-order traffic models. The traffic flow is modelled by the PW equations by a non-homogeneous system in the form of eq. (1) as:

$$\partial_t \begin{bmatrix} \rho \\ q \end{bmatrix} + \partial_x \begin{bmatrix} q \\ \frac{q^2}{\rho} + P(\rho) \end{bmatrix} = \begin{bmatrix} 0 \\ \frac{\rho V_e(\rho) - q}{\tau} \end{bmatrix}, \quad (\text{A.6})$$

where $\rho(t, x)$ is the car density, as in the LWR model; see eq. (A.2). However, here the velocity $v(t, x)$ is not only density-dependent, and is instead modelled by the second PW equation through the momentum $q(t, x) = \rho(t, x)v(t, x)$; we use the momentum equation to obtain a system in a conservative form. The PW equations in eq. (A.6) include a source term and a density-dependent traffic pressure term $P \equiv P(\rho)$, which is given by:

$$P(\rho) = \frac{V_0 - V_e(\rho)}{2\tau}, \quad (\text{A.7})$$

where τ expresses the speed relaxation time and $V_0/(2\tau)$ is a constant term, such that the pressure is zero when $\rho \rightarrow 0$.

The PW equations in eqs. (A.6) and (A.7) consist a class of macroscopic second-order traffic models which take into account the individual behavior of the driver [31, 74]. This is incorporated by the selection of microscopic velocity function $V_e(\rho)$, which is usually determined over experimental data from individual cars [74]. Here, we consider the optimal velocity (OV) function [2], reading:

$$V_e(\rho) = V(\rho^{-1}) = v_0 \frac{\tanh(\gamma\rho^{-1} - \beta) + \tanh(\beta)}{1 + \tanh(\beta)}, \quad (\text{A.8})$$

where v_0 , γ and β are parameters of the individualistic car description, expressing the desired speed, the transition width and the form factor, respectively [74]. Selecting the OV function implies that $V_0 = v_0$ in the pressure term of eq. (A.7).

For our simulations, we consider a city scenario with $\tau = 0.65$ s, $v_0 = 15$ m/s, $\gamma = 1/8$ m $^{-1}$ and $\beta = 1.5$ [74], in a road of length $L = 800$ m. First, we rescale the PW equations, so that $\rho = \mathcal{O}(1)$, and then we numerically solve them in the 1-dim. spatial domain $x \in [0, L]$ with periodic boundary conditions (a ring road), along the time interval $t \in [0, 600]$. In particular, we consider $N = 100$ cells and a, CFL satisfying, time step $dt = 0.5$. To generate the data, we consider 4 different initial conditions following a sinusoidal perturbation $\rho(0, x) = \rho^*(1 + \mu \sin(2\pi x/L))$ of a free flow density $\rho^* = 0.1$, for a uniformly varying $\mu \in [0.1, 0.4]$ with $d\mu = 0.1$; the momentum is set to $q(0, x) = 0.1$.

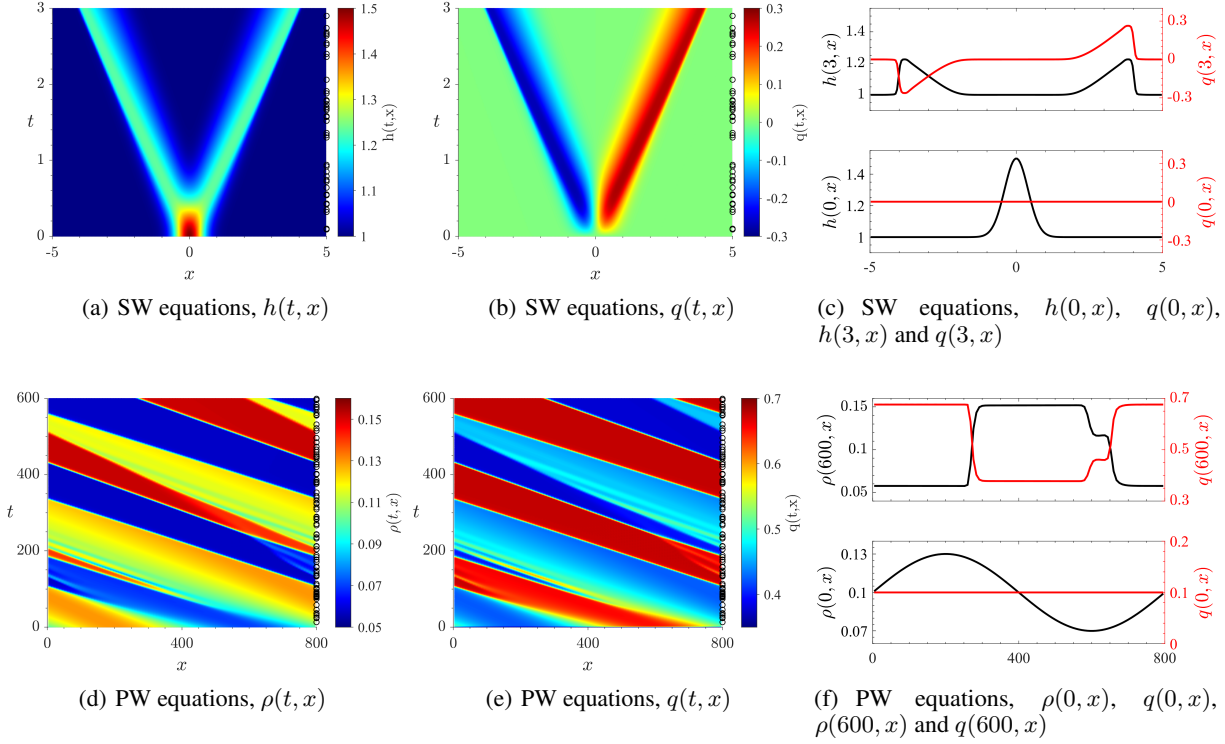


Figure A.2: Numerical solution of the SW (depth, momentum) and PW (density, momentum) equations obtained with the high-resolution Godunov-scheme in section 3.1 for (a,b,c) $x \in [-5, 5]$, $t \in [0, 3]$, with the initial data $h(0, x) = 0.5 \exp(-x^2/(2 \cdot 0.4^2))$ and $q(0, x) = 0$ shown in panel (c), and (d,e,f) $x \in [0, 800]$, $t \in [0, 600]$, with the initial data $\rho(0, x) = 0.1 (1 + 0.3 \sin(2\pi x/L))$ and $q(0, x) = 0.1$ shown in panel (f). Periodic boundary conditions are used for both SW and PW equations. The black circles on (a,b,c,d) denote the time steps n_t , collected from the depicted numerical solutions, to form the training set of GoRINNs.

Starting from the aforementioned smooth initial conditions, the PW equations develop travelling waves for the parameter set considered; such a behavior has been reported in agent-based, OV function considering, car-following models [51, 58]. During the transition to the travelling waves, the formed contact discontinuities include transonic rarefactions. Hence, for obtaining the numerical solution via the Godunov-scheme in section 3.1, the Roe solver is insufficient and thus we employed the HLLE one. The latter solver also requires the Roe matrix which, for the PW equations, is:

$$\hat{\mathbf{A}}_{i-1/2} = \begin{bmatrix} 0 & 1 \\ -\bar{q}^2 - \bar{V} & \frac{2\bar{q}}{\bar{\rho}} \end{bmatrix}, \text{ where } \bar{\rho} = \frac{\rho_l + \rho_r}{2}, \bar{q} = \bar{\rho} \frac{q_l \rho_l^{-1/2} + q_r \rho_r^{-1/2}}{\rho_l^{1/2} + \rho_r^{1/2}}, \bar{V} = \frac{V(\rho_l^{-1}) - V(\rho_r^{-1})}{2\tau(\rho_l - \rho_r)}. \quad (\text{A.9})$$

For the derivation of $\hat{\mathbf{A}}_{i-1/2}$, we followed the general approach introduced by [66], as presented in detail in appendix C.4. The resulting numerical solution of the PW equations, using the Van-Leer flux-limiter function, for the sinusoidal initial data with $\mu = 0.3$ is depicted in Figure A.2d,e,f for ρ and q , respectively. It is therein shown that the initial pulse gradually forms a left going shock wave, shown by the abrupt difference of low (high) values of ρ (q) to high (low) ones. Trailing to the right of the travelling shock wave, fluctuations develop which after $t > 500$ lead to the development of another left going shock, with the opposite behavior; abrupt differences from high (low) values of ρ (q) to low (high) ones. From the 4 numerical solutions of the PW equations, we randomly split the 7.5-7.5-85% of the time-series data to form the training/validation/testing data sets of the GoRINNs, as discussed in section 3.3; the training samples collected from the solution with initial data with $\mu = 0.3$ are denoted with black circles in Figure A.2d,e.

B Approximate Riemann solvers: Roe and HLLE solvers

As discussed in section 3, to locally approximate the solution of the Riemann problem with a contact discontinuity between the left and right states \mathbf{q}_l and \mathbf{q}_r , a linearized matrix $\hat{\mathbf{A}}_{i-1/2} \equiv \hat{\mathbf{A}}_{i-1/2}(\mathbf{q}_l, \mathbf{q}_r)$ should be derived for the non-linear system of PDEs in eq. (1), with the following properties [41, 66]:

- (i) $\hat{\mathbf{A}}_{i-1/2}(\mathbf{q}_l, \mathbf{q}_r) \rightarrow \partial_{\mathbf{u}} \mathbf{f}(\hat{\mathbf{q}})$ as $\mathbf{q}_l, \mathbf{q}_r \rightarrow \hat{\mathbf{q}}$, for consistency with the original non-linear system of PDEs,
- (ii) $\hat{\mathbf{A}}_{i-1/2}(\mathbf{q}_l, \mathbf{q}_r)$ diagonalizable with real eigenvalues, for hyperbolicity of the linearized system in eq. (8), and
- (iii) $\hat{\mathbf{A}}_{i-1/2}(\mathbf{q}_l, \mathbf{q}_r) \cdot (\mathbf{q}_r - \mathbf{q}_l) = \mathbf{f}(\mathbf{q}_r) - \mathbf{f}(\mathbf{q}_l)$, for ensuring that a Godunov-type numerical scheme, when employed to the linearized system in eq. (8), is conservative (RH condition for systems).

The first two are essential for any linearized Riemann solver, and the latter one characterizes a Roe solver; when all three properties are satisfied, $\hat{\mathbf{A}}_{i-1/2}$ is called Roe matrix.

For the construction of a Roe matrix [66], one approach is to integrate the Jacobian matrix $\partial_{\mathbf{u}} \mathbf{f}(\mathbf{u})$ over a suitable path between \mathbf{q}_l and \mathbf{q}_r , since it satisfies the first and the third properties. By considering the line path $\mathbf{u}(\xi) = \mathbf{q}_l + (\mathbf{q}_r - \mathbf{q}_l)\xi$ for $0 < \xi < 1$, the flux function difference can be written as [41]:

$$\mathbf{f}(\mathbf{q}_r) - \mathbf{f}(\mathbf{q}_l) = \left[\int_0^1 \partial_{\mathbf{u}} \mathbf{f}(\mathbf{u}(\xi)) d\xi \right] (\mathbf{q}_r - \mathbf{q}_l), \quad (\text{B.1})$$

and thus define $\hat{\mathbf{A}}_{i-1/2} = \int_0^1 \partial_{\mathbf{u}} \mathbf{f}(\mathbf{u}(\xi)) d\xi$. However, this selection doesn't necessarily satisfy the second property of hyperbolicity. More importantly, the integrals of the Jacobian matrix cannot be computed in a closed form. To overcome these obstacles, average functions of the left and right states \mathbf{q}_r and \mathbf{q}_l are frequently used (the simplest one being the arithmetic average) for defining an average state $\bar{\mathbf{q}}$ on the interface $i - 1/2$, upon which the Roe matrix is computed. This idea was first introduced by Roe in [66], resulting in the linearization approach briefly described below.

B.1 Roe solver

Roe [66] introduced a change of state variables $\mathbf{z}(\mathbf{u})$ that leads to simpler integral expressions. In addition, this mapping is invertible, allowing us to derive $\mathbf{u}(\mathbf{z})$, and thus cast the flux function as $\mathbf{f}(\mathbf{u}(\mathbf{z})) = \mathbf{f}(\mathbf{z})$. Then, one can integrate along the line path $\mathbf{z}(\xi) = \mathbf{z}_l + (\mathbf{z}_r - \mathbf{z}_l)\xi$ for $0 < \xi < 1$, where $\mathbf{z}_{l,r} = \mathbf{z}(\mathbf{q}_{l,r})$. Since $\partial_{\xi} \mathbf{z}(\xi) = \mathbf{z}_r - \mathbf{z}_l$, the flux function difference now takes the form [41]:

$$\mathbf{f}(\mathbf{q}_r) - \mathbf{f}(\mathbf{q}_l) = \left[\int_0^1 \partial_{\mathbf{z}} \mathbf{f}(\mathbf{z}(\xi)) d\xi \right] (\mathbf{z}_r - \mathbf{z}_l) = \hat{\mathbf{C}}_{i-1/2} (\mathbf{z}_r - \mathbf{z}_l), \quad (\text{B.2})$$

where $\hat{\mathbf{C}}_{i-1/2} \in \mathbb{R}^{D \times D}$ includes the integrals of each component of $\partial_{\mathbf{z}} \mathbf{f}(\mathbf{z}(\xi))$. A parsimonious selection of $\mathbf{z}(\mathbf{u})$ makes these integrals computable in a closed form. Now, given that $\mathbf{z}(\mathbf{u})$ is invertible, one easily derives:

$$\mathbf{q}_r - \mathbf{q}_l = \left[\int_0^1 \partial_{\mathbf{z}} \mathbf{u}(\mathbf{z}(\xi)) d\xi \right] (\mathbf{z}_r - \mathbf{z}_l) = \hat{\mathbf{B}}_{i-1/2} (\mathbf{z}_r - \mathbf{z}_l), \quad (\text{B.3})$$

where $\hat{\mathbf{B}}_{i-1/2} \in \mathbb{R}^{D \times D}$ includes the integrals of each component of $\partial_{\mathbf{z}} \mathbf{u}(\mathbf{z}(\xi))$. Following eqs. (B.2) and (B.3), the desired matrix is computed as $\hat{\mathbf{A}}_{i-1/2} = \hat{\mathbf{C}}_{i-1/2} \hat{\mathbf{B}}_{i-1/2}^{-1}$, and satisfies the third property that $\hat{\mathbf{A}}_{i-1/2}$ should possess. Usually the first property is also satisfied, while the second one (regarding hyperbolicity) holds, under specific conditions of the entropy function [30], which are not explored in this work.

Alternatively to the above general derivation of $\hat{\mathbf{A}}_{i-1/2}$ [41], a "reverse engineering" approach was introduced in [35], which finds some *average* state $\bar{\mathbf{q}}$ as a function of \mathbf{q}_r and \mathbf{q}_l , such that $\hat{\mathbf{A}}_{i-1/2}(\mathbf{q}_l, \mathbf{q}_r) = \partial_{\mathbf{u}} \mathbf{f}(\bar{\mathbf{q}})$. This selection satisfies by definition the first property, and also the third one, when the average state $\bar{\mathbf{q}}$ is computed via:

$$\partial_{\mathbf{u}} \mathbf{f}(\bar{\mathbf{q}}) \cdot (\mathbf{q}_r - \mathbf{q}_l) = \mathbf{f}(\mathbf{q}_r) - \mathbf{f}(\mathbf{q}_l) \quad (\text{B.4})$$

This technique usually results in the same matrices $\hat{\mathbf{A}}_{i-1/2}$ as the ones derived by eqs. (B.2) and (B.3) in [41], as was the case for all the benchmark problems considered in this work, except from the PW equations, where the later alternative technique cannot be employed due to the non-linear flux function. We hereby note that the Roe linearized matrix for the Burger's, LWR and SW system of PDEs was cross-validated with expressions provided in [35, 41], while for the PW system, it was derived in this work.

B.2 HLLE solver

In cases where the Roe linearization fails, the HLLE solver, introduced in [23, 30], can be used as an alternative approximate Riemann solver. According to the HLLE solver, the Riemann problem is approximated by only two waves, propagating with the smallest and largest speeds:

$$s_{i-1/2}^1 = \min_p(\min(\lambda_{i-1}^p, \hat{\lambda}_{i-1/2}^p)), \quad s_{i-1/2}^2 = \max_p(\max(\lambda_i^p, \hat{\lambda}_{i-1/2}^p)) \quad (\text{B.5})$$

where λ_{i-1}^p and λ_i^p are the p -th eigenvalues of the Jacobian $\partial \mathbf{f}(\mathbf{u}) / \partial \mathbf{u}$ at \mathbf{q}_l and \mathbf{q}_r respectively, while $\hat{\lambda}_{i-1/2}^p$ is the p -th eigenvalue of the $\hat{\mathbf{A}}_{i-1/2}$ derived via Roe linearization. Using the above selection, the middle state of the Riemann problem's approximate solution is then computed as:

$$\mathbf{q}_m = \frac{\mathbf{f}(\mathbf{q}_r) - \mathbf{f}(\mathbf{q}_l) - s_{i-1/2}^2 \mathbf{q}_r + s_{i-1/2}^1 \mathbf{q}_l}{s_{i-1/2}^1 - s_{i-1/2}^2}, \quad (\text{B.6})$$

that is also conservative. In turn, the two waves are approximated as:

$$\mathbf{W}_{i-1/2}^1 = \mathbf{q}_m - \mathbf{q}_l, \quad \mathbf{W}_{i-1/2}^2 = \mathbf{q}_r - \mathbf{q}_m. \quad (\text{B.7})$$

The HLLE solver performs similarly to the Roe solver, without however requiring the entropy fixes that the latter requires when facing rarefaction waves (see [41]). However, the HLLE solver includes only $M_w = 2$ waves, which may affect the resolution of systems with more than two variables. In this work, this solver was only employed for the PW system of hyperbolic PDEs.

C Roe solvers for the benchmark problems

Here, we provide the expressions of the Roe matrices and the resulting speeds and waves used in the - Roe/HLLE solver based - FV high-resolution Godunov-type method for each benchmark problem considered.

C.1 The Burger's equation

Recall that the Burger's equation in eq. (A.1) is written in the form of a scalar PDE in eq. (1), where

$$\mathbf{u} = u, \quad \mathbf{f}(\mathbf{u}) = u^2/2, \quad \partial_{\mathbf{u}} \mathbf{f}(\mathbf{u}) = u. \quad (\text{C.1})$$

Since this is a scalar hyperbolic PDE, the Roe matrix is scalar, say $\hat{a}_{i-1/2}$, and is provided by the following proposition:

Proposition C.1. [41] *The Roe matrix of the Burger's equation in eq. (A.1) is the simple arithmetic average:*

$$\hat{a}_{i-1/2} = (u_r + u_l)/2. \quad (\text{C.2})$$

Proof. Following the “reverse engineering” technique presented in appendix B.1, we solve eq. (B.4) to define $\bar{\mathbf{q}} = \bar{u}$, which implies:

$$\bar{u}(u_r - u_l) = (u_r^2 - u_l^2)/2 \Rightarrow \bar{u} = (u_r + u_l)/2. \quad (\text{C.3})$$

The resulting scalar $\hat{a}_{i-1/2} = \bar{u} = (u_r + u_l)/2$ satisfies all three properties of a Roe matrix, as discussed in appendix B.1, since (i) $\hat{a}_{i-1/2}(u_l, u_r) \rightarrow \partial_{\mathbf{u}} \mathbf{f}(\hat{u})$ as $u_l, u_r \rightarrow \hat{u}$, (ii) $\hat{a}_{i-1/2} \in \mathbb{R}$ and (iii) the RH condition is satisfied by construction. \square

To perform the FV update in eq. (6) with the Roe solver, we set $u_l = \mathbf{Q}_{i-1}^n$ and $u_r = \mathbf{Q}_i^n$ at the n -th time step and i -th cell, and compute, from the Roe matrix $\hat{a}_{i-1/2}$ in eq. (C.2), the speed $s_{i-1/2}^p = \hat{a}_{i-1/2}$ and the wave $\mathbf{W}_{i-1/2}^p = u_r - u_l$ for $p = 1$.

C.2 The LWR equation of traffic flow

Recall that the scalar PDE of the LWR model in eq. (A.2) is written in the form of eq. (1), where

$$\mathbf{u} = \rho, \quad \mathbf{f}(\mathbf{u}) = \rho v(\rho), \quad \partial_{\mathbf{u}} \mathbf{f}(\mathbf{u}) = v(\rho) + \rho v'(\rho), \quad (\text{C.4})$$

for $v(\rho) = v_{max}(1 - \rho)$ and $v'(\rho) = -v_{max}$. Since the LWR model is a scalar hyperbolic PDE, the Roe matrix is scalar as well, say $\hat{a}_{i-1/2}$, and is provided by the following proposition:

Proposition C.2. [41] The Roe matrix of the LWR equation in eq. (A.2) is:

$$\hat{a}_{i-1/2} = v_{max}(1 - \rho_r - \rho_l). \quad (\text{C.5})$$

Proof. Following the “reverse engineering” technique presented in appendix B.1, we solve eq. (B.4) to define $\bar{\mathbf{q}} = \bar{\rho}$, which implies:

$$(v(\bar{\rho}) + \bar{\rho}v'(\bar{\rho}))(\rho_r - \rho_l) = \rho_r v(\rho_r) - \rho_l v(\rho_l) \quad (\text{C.6})$$

After some calculations, the above equation results to the common average $\bar{\rho} = (\rho_r + \rho_l)/2$ for any $v_{max} > 0$ and thus, $\hat{a}_{i-1/2}$ is given by

$$\hat{a}_{i-1/2} = v(\bar{\rho}) + \bar{\rho}v'(\bar{\rho}) = v_{max}(1 - 2\bar{\rho}). \quad (\text{C.7})$$

The resulting $\hat{a}_{i-1/2}$ satisfies all three properties of a Roe matrix, as discussed in appendix B.1, since (i) $\hat{a}_{i-1/2}(\rho_l, \rho_r) \rightarrow \partial_\rho \mathbf{f}(\hat{\rho})$ as $\rho_l, \rho_r \rightarrow \hat{\rho}$, (ii) $\hat{a}_{i-1/2} \in \mathbb{R}^N$, and (iii) the RH condition is satisfied by construction. \square

Similarly to the Burger’s equation, to perform the FV update in eq. (6) with the Roe solver, we set $\rho_l = \mathbf{Q}_{i-1}^n$ and $\rho_r = \mathbf{Q}_i^n$ at the n -th time step and i -th cell, and compute, from the Roe matrix $\hat{a}_{i-1/2}$ in eq. (C.5), the speed $s_{i-1/2}^p = \hat{a}_{i-1/2}$ and the wave $\mathbf{W}_{i-1/2}^p = \rho_r - \rho_l$ for $p = 1$.

C.3 The SW equations

As a reminder, recall that the SW system of PDEs in eq. (A.4) is written in the form of eq. (1), where

$$\mathbf{u} = \begin{bmatrix} h \\ q \end{bmatrix}, \quad \mathbf{f}(\mathbf{u}) = \begin{bmatrix} q \\ \frac{q^2}{h} + \frac{1}{2}gh^2 \end{bmatrix}, \quad \partial_{\mathbf{u}} \mathbf{f}(\mathbf{u}) = \begin{bmatrix} 0 & 1 \\ -\frac{q^2}{h^2} + gh & \frac{2q}{h} \end{bmatrix}. \quad (\text{C.8})$$

The Roe matrix of the SW system is provided by the following proposition:

Proposition C.3. [41] The Roe matrix of the SW equations in eq. (A.4) is:

$$\hat{\mathbf{A}}_{i-1/2} = \begin{bmatrix} 0 & 1 \\ -\frac{\bar{q}^2}{\bar{h}^2} + g\bar{h} & 2\frac{\bar{q}}{\bar{h}} \end{bmatrix}, \quad \text{where} \quad \bar{h} = \frac{h_l + h_r}{2}, \quad \bar{q} = \bar{h} \frac{q_l h_l^{-1/2} + q_r h_r^{-1/2}}{h_l^{1/2} + h_r^{1/2}}, \quad (\text{C.9})$$

Proof. Following the technique described in appendix B.1, as introduced in [66], we employ the change of variables $\mathbf{z}(\mathbf{u}) = h^{-1/2}\mathbf{u}$. This mapping is reversible, resulting to:

$$\mathbf{z}(\mathbf{u}) = \begin{bmatrix} z^1 \\ z^2 \end{bmatrix} = \begin{bmatrix} h^{1/2} \\ qh^{-1/2} \end{bmatrix}, \quad \mathbf{u}(\mathbf{z}) = \begin{bmatrix} (z^1)^2 \\ z^1 z^2 \end{bmatrix} \Rightarrow \partial_{\mathbf{z}} \mathbf{u}(\mathbf{z}) = \begin{bmatrix} 2z^1 & 0 \\ z^2 & z^1 \end{bmatrix}. \quad (\text{C.10})$$

Now, the flux function and its Jacobian is written in terms of \mathbf{z} as:

$$\mathbf{f}(\mathbf{z}) = \begin{bmatrix} z^1 z^2 \\ (z^2)^2 + \frac{1}{2}g(z^1)^4 \end{bmatrix}, \quad \partial_{\mathbf{z}} \mathbf{f}(\mathbf{z}) = \begin{bmatrix} z^2 & z^1 \\ 2g(z^1)^3 & 2z^2 \end{bmatrix}. \quad (\text{C.11})$$

Next, setting the line path $z^p(\xi) = z_l^p + (z_r^p - z_l^p)\xi$ for $p = 1, 2$, the integration of all elements of the matrices in eqs. (C.10) and (C.11) is straightforward, resulting to:

$$\hat{\mathbf{B}}_{i-1/2} = \begin{bmatrix} 2\bar{Z}^1 & 0 \\ \bar{Z}^2 & \bar{Z}^1 \end{bmatrix}, \quad \hat{\mathbf{C}}_{i-1/2} = \begin{bmatrix} \bar{Z}^2 & \bar{Z}^1 \\ 2g\bar{Z}^1\bar{h} & 2\bar{Z}^2 \end{bmatrix}, \quad (\text{C.12})$$

where $\bar{Z}^p = (z_l^p + z_r^p)/2$ and $\bar{h} = (h_l + h_r)/2$. Thus, the matrix $\hat{\mathbf{A}}_{i-1/2}$ takes the form:

$$\hat{\mathbf{A}}_{i-1/2} = \hat{\mathbf{C}}_{i-1/2} \hat{\mathbf{B}}_{i-1/2}^{-1} = \begin{bmatrix} 0 & 1 \\ -\frac{\bar{q}^2}{\bar{h}^2} + g\bar{h} & \frac{2\bar{q}}{\bar{h}} \end{bmatrix}, \quad (\text{C.13})$$

where

$$\bar{q} = \bar{h} \frac{q_l h_l^{-1/2} + q_r h_r^{-1/2}}{h_l^{1/2} + h_r^{1/2}}. \quad (\text{C.14})$$

For the computation of $\hat{\mathbf{A}}_{i-1/2}$, one can alternatively follow the “reverse engineering” technique presented in appendix B and solve eq. (B.4) for $\bar{\mathbf{q}} = (\bar{h}, \bar{q})$, as done in [35]. This procedure implies the same average states, \bar{h} and \bar{q} , found above, and thus results to the same $\hat{\mathbf{A}}_{i-1/2}$ matrix of eq. (C.13).

The resulting $\hat{\mathbf{A}}_{i-1/2}$ in eq. (C.13) is the Jacobian $\partial_{\mathbf{u}} \mathbf{f}(\mathbf{u})$ evaluated in (\bar{h}, \bar{q}) . This implies that the property (i) in appendix B is satisfied; i.e., when $(h_l, q_l), (h_r, q_r) \rightarrow (\hat{h}, \hat{q})$, then $\bar{h} \rightarrow \hat{h}$ and $\bar{q} \rightarrow \hat{q}$, so that $\hat{\mathbf{A}}_{i-1/2}((h_l, q_l), (h_r, q_r)) \rightarrow \partial_{(h,q)} \mathbf{f}(\hat{h}, \hat{q})$. In addition, the matrix $\hat{\mathbf{A}}_{i-1/2}$ in eq. (C.13) has always real eigenvalues, thus satisfying property (ii) in appendix B. This is because:

$$\text{Tr}(\hat{\mathbf{A}}_{i-1/2})^2 - 4\text{Det}(\hat{\mathbf{A}}_{i-1/2}) = 4g\bar{h} \geq 0, \quad (\text{C.15})$$

since $g > 0$ and $\bar{h} \geq 0$. Finally, as shown in appendix B.1, the matrix $\hat{\mathbf{A}}_{i-1/2}$ also satisfies the RH condition by construction. Hence, all three properties in appendix B are satisfied, defining $\hat{\mathbf{A}}_{i-1/2}$ in eq. (C.13) a Roe matrix. \square

The eigenvalues $\hat{\lambda}_{i-1/2}^{1,2}$ and the eigenvectors $\hat{\mathbf{r}}_{i-1/2}^{1,2}$ of the matrix $\hat{\mathbf{A}}_{i-1/2}$ can be computed analytically as:

$$\hat{\lambda}_{i-1/2}^{1,2} = \frac{\bar{q}}{\bar{h}} \pm \sqrt{g\bar{h}}, \quad \hat{\mathbf{r}}_{i-1/2}^{1,2} = \begin{bmatrix} 1 \\ \frac{\bar{q}}{\bar{h}} \pm \sqrt{g\bar{h}} \end{bmatrix}. \quad (\text{C.16})$$

Hence, to perform the FV update in eq. (6) with the Roe solver, we set $(h_l, q_l)^\top = \mathbf{Q}_{i-1}^n$ and $(h_r, q_r)^\top = \mathbf{Q}_i^n$ at the n -th time step and i -th cell, and compute (i) the speeds $s_{i-1/2}^p$ by the eigenvalues $\hat{\lambda}_{i-1/2}^p$ in eq. (C.16) and, (ii) the waves $\mathbf{W}_{i-1/2}^p$ (computed via the eigenvectors in eq. (C.16)) by the expressions:

$$\mathbf{W}_{i-1/2}^p = a_{i-1/2}^p \hat{\mathbf{r}}_{i-1/2}^p, \quad \text{where } \mathbf{a}_{i-1/2} = \begin{bmatrix} a_{i-1/2}^1 \\ a_{i-1/2}^2 \end{bmatrix} = [\hat{\mathbf{r}}_{i-1/2}^1 \quad \hat{\mathbf{r}}_{i-1/2}^2]^{-1} \begin{bmatrix} h_r - h_l \\ q_r - q_l \end{bmatrix} \quad (\text{C.17})$$

for $p = 1, 2$.

C.4 The PW equations

Recall that the system of PDEs provided by the PW model in eq. (A.6) with the use of the optimal velocity function is written in the form of eq. (1) where

$$\mathbf{u} = \begin{bmatrix} \rho \\ q \end{bmatrix}, \quad \mathbf{f}(\mathbf{u}) = \begin{bmatrix} q \\ \frac{q^2}{\rho} + \frac{V_0 - V(\rho^{-1})}{2\tau} \end{bmatrix}, \quad \partial_{\mathbf{u}} \mathbf{f}(\mathbf{u}) = \begin{bmatrix} 0 & 1 \\ -\frac{q^2}{\rho^2} + \frac{V'(\rho^{-1})}{2\tau\rho^2} & \frac{2q}{\rho} \end{bmatrix} \quad (\text{C.18})$$

where $V'(\cdot)$ denotes the derivative of the optimal velocity function. The respective Roe matrix is provided by the following proposition:

Proposition C.4. *The Roe matrix of the PW equations in eq. (A.6) is:*

$$\hat{\mathbf{A}}_{i-1/2} = \begin{bmatrix} 0 & 1 \\ -\frac{\bar{q}^2}{\bar{\rho}^2} - \bar{V} & 2\bar{q} \end{bmatrix}, \quad \text{where } \bar{\rho} = \frac{\rho_l + \rho_r}{2}, \quad \bar{q} = \bar{\rho} \frac{q_l \rho_l^{-1/2} + q_r \rho_r^{-1/2}}{\rho_l^{1/2} + \rho_r^{1/2}}, \quad \bar{V} = \frac{V(\rho_l^{-1}) - V(\rho_r^{-1})}{2\tau(\rho_l - \rho_r)}. \quad (\text{C.19})$$

Proof. Following the technique described in appendix B.1, as introduced in [66], we employ the change of variables $\mathbf{z}(\mathbf{u}) = \rho^{-1/2} \mathbf{u}$, inspired by the shallow water Roe linearization. This mapping is reversible, resulting to:

$$\mathbf{z}(\mathbf{u}) = \begin{bmatrix} z^1 \\ z^2 \end{bmatrix} = \begin{bmatrix} \rho^{1/2} \\ q \rho^{-1/2} \end{bmatrix}, \quad \mathbf{u}(\mathbf{z}) = \begin{bmatrix} (z^1)^2 \\ z^1 z^2 \end{bmatrix} \Rightarrow \partial_{\mathbf{z}} \mathbf{u}(\mathbf{z}) = \begin{bmatrix} 2z^1 & 0 \\ z^2 & z^1 \end{bmatrix}. \quad (\text{C.20})$$

Now, the flux function and its Jacobian is written in terms of \mathbf{z} as:

$$\mathbf{f}(\mathbf{z}) = \begin{bmatrix} z^1 z^2 \\ (z^2)^2 + \frac{V_0 - V((z^1)^{-2})}{2\tau} \end{bmatrix}, \quad \partial_{\mathbf{z}} \mathbf{f}(\mathbf{z}) = \begin{bmatrix} z^2 & z^1 \\ \frac{V'((z^1)^{-2})}{\tau(z^1)^3} & 2z^1 \end{bmatrix}. \quad (\text{C.21})$$

Next, setting the line path $z^p(\xi) = z_l^p + (z_r^p - z_l^p)\xi$ for $p = 1, 2$, the integration of all elements of the matrices in eqs. (C.20) and (C.21) is straightforward, except only from the bottom left element of the matrix in eq. (C.21), which is integrated as:

$$\begin{aligned} \int_0^1 \frac{V'((z^1(\xi))^{-2})}{\tau(z^1(\xi))^3} d\xi &= \int_0^1 -\frac{1}{2\tau} \frac{dV((z^1(\xi))^2)}{dz^1(\xi)} d\xi = -\frac{1}{2\tau} \int_0^1 \left(\frac{dV((z^1(\xi))^2)}{d\xi} \right) \left(\frac{dz^1(\xi)}{d\xi} \right)^{-1} d\xi = \\ &= -\frac{1}{2\tau(z_l^1 - z_r^1)} \int_0^1 \frac{dV((z^1(\xi))^2)}{d\xi} d\xi = -\frac{V((z_r^1)^2) - V((z_l^1)^2)}{2\tau(z_r^1 - z_l^1)} \equiv -\hat{V}, \end{aligned} \quad (\text{C.22})$$

where the chain rule is employed at the third step of the above calculation. Then, the matrices in eqs. (C.20) and (C.21) are computed as:

$$\hat{\mathbf{B}}_{i-1/2} = \begin{bmatrix} 2\bar{Z}^1 & 0 \\ \bar{Z}^2 & \bar{Z}^1 \end{bmatrix}, \quad \hat{\mathbf{C}}_{i-1/2} = \begin{bmatrix} \bar{Z}^2 & \bar{Z}^1 \\ -\hat{V} & 2\bar{Z}^2 \end{bmatrix}, \quad (\text{C.23})$$

where $\bar{Z}^p = (Z_{i-1}^p + Z_i^p)/2$. Returning to the original variables \mathbf{u} , the matrix $\hat{\mathbf{A}}_{i-1/2}$ takes the form:

$$\hat{\mathbf{A}}_{i-1/2} = \hat{\mathbf{C}}_{i-1/2} \hat{\mathbf{B}}_{i-1/2}^{-1} = \begin{bmatrix} 0 & 1 \\ -\frac{\bar{q}^2}{\bar{\rho}^2} - \bar{V} & \frac{2\bar{q}}{\bar{\rho}} \end{bmatrix}, \quad (\text{C.24})$$

where

$$\bar{\rho} = \frac{\rho_l + \rho_r}{2}, \quad \bar{q} = \bar{\rho} \frac{q_l \rho_l^{-1/2} + q_r \rho_r^{-1/2}}{\rho_l^{1/2} + \rho_r^{1/2}}, \quad \bar{V} = \frac{V(\rho_l^{-1}) - V(\rho_r^{-1})}{2\tau(\rho_l - \rho_r)}. \quad (\text{C.25})$$

Note that \bar{V} is not ill-conditioned and, in fact,

$$\bar{V} \rightarrow -\frac{1}{2\tau\hat{\rho}^2} \frac{\partial V(\hat{\rho}^{-1})}{\partial \rho} \in \mathbb{R}, \quad \text{as} \quad \rho_l, \rho_r \rightarrow \hat{\rho}. \quad (\text{C.26})$$

In contrast to the SW system of PDEs, here the matrix $\hat{\mathbf{A}}_{i-1/2}$ in eq. (C.19) is not the Jacobian evaluated in $(\bar{\rho}, \bar{q})$. It is in fact impossible to derive the Roe matrix following the alternative technique presented in appendix B, due to the non-linearity of the optimal velocity function, that hinders the derivation of $(\bar{\rho}, \bar{q})$.

Nonetheless, the matrix $\hat{\mathbf{A}}_{i-1/2}$ in eq. (C.24) satisfies property (i) in appendix B; i.e., when $(\rho_l, q_l), (\rho_r, q_r) \rightarrow (\hat{\rho}, \hat{q})$, then $\bar{\rho} \rightarrow \hat{\rho}$, $\bar{q} \rightarrow \hat{q}$ and $\bar{V} \rightarrow -\frac{V'(\hat{\rho}^{-1})}{2\tau\hat{\rho}^2}$ as shown in eq. (C.26), implying that $\hat{\mathbf{A}}_{i-1/2}((\rho_l, q_l), (\rho_r, q_r)) \rightarrow \partial_{(\rho, q)} \mathbf{f}(\hat{\rho}, \hat{q})$. In addition, the matrix $\hat{\mathbf{A}}_{i-1/2}$ in eq. (C.24) has always real eigenvalues, thus satisfying property (ii) in appendix B. This is because:

$$\text{Tr}(\hat{\mathbf{A}}_{i-1/2})^2 - 4\text{Det}(\hat{\mathbf{A}}_{i-1/2}) = \frac{2v_0(\tanh(\beta - \gamma\rho_r^{-1}) - \tanh(\beta - \gamma\rho_l^{-1}))}{\tau(1 + \tanh(\beta))(\rho_r - \rho_l)} \geq 0 \quad (\text{C.27})$$

for any $\rho_r \neq \rho_l \geq 0$, since $\gamma > 0$, $v_0/(\tau(1 + \tanh(\beta))) > 0$ and $\tanh(\cdot)$ is a monotonically increasing function. Note that when $\rho_r = \rho_l$, one should use the limit in eq. (C.26) to construct the matrix $\hat{\mathbf{A}}_{i-1/2}$. Finally, as shown in appendix B.1, the matrix $\hat{\mathbf{A}}_{i-1/2}$ also satisfies the RH condition by construction. Hence, all three properties in appendix B are satisfied, making $\hat{\mathbf{A}}_{i-1/2}$ in eq. (C.24) a Roe matrix. \square

The eigenvalues $\hat{\lambda}_{i-1/2}^{1,2}$ and the eigenvectors $\hat{\mathbf{r}}_{i-1/2}^{1,2}$ of the matrix $\hat{\mathbf{A}}_{i-1/2}$ can be computed analytically as:

$$\hat{\lambda}_{i-1/2}^{1,2} = \frac{\bar{q}}{\bar{\rho}} \pm \sqrt{-\bar{V}}, \quad \hat{\mathbf{r}}_{i-1/2}^{1,2} = \begin{bmatrix} 1 \\ \frac{\bar{q}}{\bar{\rho}} \pm \sqrt{-\bar{V}} \end{bmatrix}. \quad (\text{C.28})$$

Hence, to perform the FV update in eq. (6) with the Roe solver, (i) the speeds $s_{i-1/2}^p$ are provided by the eigenvalues $\hat{\lambda}_{i-1/2}^p$ in eq. (C.28) and, (ii) the waves $\mathbf{W}_{i-1/2}^p$ (computed via the eigenvectors in eq. (C.28)) are provided by the expressions:

$$\mathbf{W}_{i-1/2}^p = a_{i-1/2}^p \hat{\mathbf{r}}_{i-1/2}^p, \quad \text{where} \quad \mathbf{a}_{i-1/2} = \begin{bmatrix} a_{i-1/2}^1 \\ a_{i-1/2}^2 \end{bmatrix} = [\hat{\mathbf{r}}_{i-1/2}^1 \quad \hat{\mathbf{r}}_{i-1/2}^2]^{-1} \begin{bmatrix} \rho_r - \rho_l \\ q_r - q_l \end{bmatrix} \quad (\text{C.29})$$

for $p = 1, 2$. For the FV update in eq. (6) with the HLLE solver, only the eigenvalues $\hat{\lambda}_{i-1/2}^p$ in eq. (C.28) are required, as shown in appendix B.2.

D Supplemental Figures for PW equation when learning $\mathcal{N}(\rho, q)$

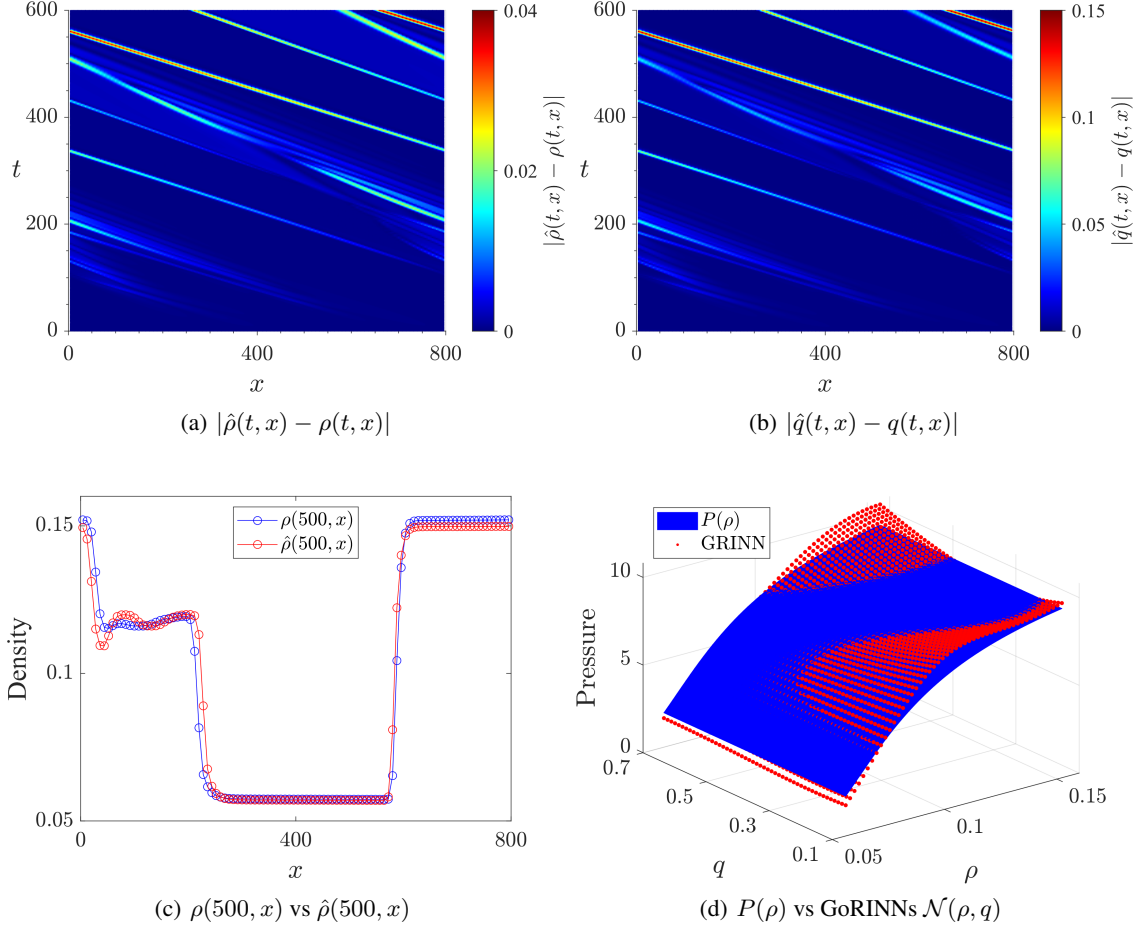


Figure D.1: Numerical accuracy of GoRINNs, assuming a pressure closure of the form $\mathcal{N}(\rho, q)$, for the PW equations. (a,b) Absolute errors of the numerical solution provided by the GoRINNs learned equations in eq. (26) ($\hat{\rho}$ and \hat{q}) vs the one provided by the PW equations in eq. (A.6) (ρ and q). (c) Solutions compared in panel (a) at $t = 500$. (d) Analytically known pressure closure $P(\rho)$ vs the $\mathcal{N}(\rho, q)$ functional learned with GoRINNs.